

Identification of hot gas around low-mass protostars

MEREL L.R. VAN 'T HOFF,¹ EDWIN A. BERGIN,¹ PENELOPE RILEY,^{2,3} SANIL MITTAL,¹ JES K. JØRGENSEN,⁴ AND JOHN J. TOBIN⁵

¹*Department of Astronomy, University of Michigan, 1085 S. University Ave., Ann Arbor, MI 48109-1107, USA*

²*Department of Physics and Astrophysics, DePaul University, Chicago, IL 60614-3504, USA*

³*Department of Astronomy, University of Illinois, 1002 West Green St., Urbana, IL 61801, USA*

⁴*Niels Bohr Institute, University of Copenhagen, Øster Voldgade 5–7, DK-1350, Copenhagen K, Denmark*

⁵*National Radio Astronomy Observatory, 520 Edgemont Rd., Charlottesville, VA 22903, USA*

ABSTRACT

The low carbon content of Earth and primitive meteorites compared to the Sun and interstellar grains suggests that carbon-rich grains were destroyed in the inner few astronomical units of the young solar system. A promising mechanism to selectively destroy carbonaceous grains is thermal sublimation within the soot line at $\gtrsim 300$ K. To address whether such hot conditions are common amongst low-mass protostars, we observe CH₃CN transitions at 1, 2 and 3 mm with the Northern Extended Millimeter Array (NOEMA) toward seven low-mass and one intermediate-mass protostar ($L_{\text{bol}} \sim 2 - 300 L_{\odot}$), as CH₃CN is an excellent temperature tracer. We find > 300 K gas toward all sources, indicating that hot gas may be prevalent. Moreover, the excitation temperature for CH₃OH obtained with the same observations is always lower (~ 135 – 250 K), suggesting that CH₃CN and CH₃OH have a different spatial distribution. A comparison of the column densities at 1 and 3 mm shows a stronger increase at 3 mm for CH₃CN than for CH₃OH. Since the dust opacity is lower at longer wavelengths, this indicates that CH₃CN is enhanced in the hot gas compared to CH₃OH. If this CH₃CN enhancement is the result of carbon-grain sublimation, these results suggest that Earth's initial formation conditions may not be rare.

1. INTRODUCTION

One aspect of determining the occurrence rate of Earth-like planets is understanding the conditions in the early solar system and the prevalence of these conditions amongst low-mass protostars. The composition of Earth can provide information about the composition of the material from which it formed, which is related to the physical conditions in the young disk. For example, since Earth is water poor, it must have formed inside the water snowline. Carbon is also informative as Earth is at least two orders of magnitude depleted in carbon compared to the Sun, interstellar grains and the two well-characterized comets 1P/Halley and 67P/Churyumov-Gerasimenko (Geiss 1987; Bergin et al. 2015; Rubin et al. 2019; Li et al. 2021). A similar amount of depletion is seen in CI chondrites, which represent the most primitive material in the solar system and otherwise reflect

solar abundances (Wasson & Kallemeyn 1988). This means that carbon had to be predominantly present in the gas phase instead of in the refractory phase in the inner young solar system, and as such, could not be efficiently accreted onto forming rocky bodies.

Oxidation processes can selectively destroy carbonaceous grains while leaving silicate grains intact, but detailed models suggest that these processes by themselves are ineffective (Anderson et al. 2017; Klarmann et al. 2018; Binkert & Birnstiel 2023). An alternative (additional) mechanism is the thermal sublimation of carbon-rich grains inside the “soot line” (Kress et al. 2010; Li et al. 2021). The exact temperature at which this sublimation occurs depends on the form of the refractory carbon, with the dominant carbon carrier ($\sim 60\%$), organic material, sublimating at temperatures between ~ 350 – 450 K (Nakano et al. 2003; Gail & Trieloff 2017). Constraints can also be placed based on the composition of meteorites (Li et al. 2021): meteoritic materials carry more carbon than water (Hirschmann & Dasgupta 2009), but less carbon than sulfur, with C/S ratios well below solar (Hirschmann 2016). This suggests that the

sublimation temperature of the main carbon carrier is between that of water ($\sim 150\text{--}200$ K; Fraser et al. 2001) and the main sulfur carrier, troilite (680 K; Pollack et al. 1994). Both results then suggest a sublimation temperature of roughly 400 K, compared to ~ 1200 K for silicates (Pollack et al. 1994).

Multiple lines of evidence suggest that carbon-grain sublimation must be active during the protostellar phase. First, grain growth already starts while the disk is still forming within an infalling envelope (e.g., Segura-Cox et al. 2020; Tychoniec et al. 2020), and smaller bodies are more easy to sublimate than larger bodies. Second, high temperatures are more easily reached during the protostellar phase when stellar accretion rates are higher and accretion bursts are more frequent. Li et al. (2021) demonstrated that temperatures were only high enough for carbon-grain sublimation at 1 au within the first couple hundred-thousand years. Since sublimation has a well characterized exponential relation between pressure and temperature, and the density in the inner region of protostellar envelopes is lower compared to the inner disk, carbon-grain sublimation is expected to occur at temperatures of $\gtrsim 300$ K around protostars (van 't Hoff et al. 2020).

van 't Hoff et al. (2020) argue that the destruction of carbon-rich grains will lead to the gas-phase formation of hydrocarbons and nitriles (molecules with a $\text{C}\equiv\text{N}$ bond, such as HCN and CH_3CN) inside the soot line (see also the chemical models by Wei et al. 2019) as, in addition to carbon, a significant fraction of the total nitrogen abundance is present in carbonaceous grains. Carbon-grain sublimation is thus expected to enhance the abundance of nitrogen-bearing complex organic molecules (N-COMs) inside the soot line while oxygen-bearing COMs (O-COMs) are expected to be present in the gas phase more uniformly out to the water snowline ($\sim 100\text{--}150$ K; Penteado et al. 2017; Ferrero et al. 2020, and references therein). This suggests that we may observe smaller emitting areas and higher excitation temperatures for N-COMs compared to O-COMs. Even in the absence of carbon-grain sublimation, some astrochemical models predict that certain reactions, such as hydrogen abstraction from ammonia, become active at $\gtrsim 300$ K, altering the chemical composition of hot gas compared to warm gas just inside the water snowline (Garrod 2013; Garrod et al. 2017, 2022).

A rich hydrocarbon chemistry and high C/O ratio, potentially due to carbon-grain destruction, was recently detected toward a low-mass disk with JWST (Tabone et al. 2023), but observational constraints on the occurrence of carbon-grain sublimation, and of hot gas more generally, around low-mass protostars are scarce. Exist-

Table 1. Overview of sources.

Source	R.A. ^a (J2000)	Dec. ^a (J2000)	Class	L_{bol} (L_{\odot})	Ref. ^b
HBC494	05:40:27.45	-07:27:29.67	I	~ 300	1
HOPS-370	05:35:27.63	-05:09:34.42	0/I	314	2
Per-emb-17	03:27:39.11	+30:13:02.93	0	7.1 ^c	3
Per-emb-20	03:27:43.28	+30:12:28.79	0/I	2.4	3
Ser-emb-1	18:29:09.09	+00:31:30.86	0	4.5	4
Ser-emb-8	18:29:48.09	+01:16:43.26	0	5.9 ^d	4
Ser-emb-11E	18:29:06.68	+00:30:33.80	0/I ^c	5.3 ^c	4
Ser-emb-11W	18:29:06.63	+00:30:33.90	0/I ^c	5.3 ^c	4
Ser-emb-17	18:29:06.21	+00:30:42.99	I	4.2	4
Ser-emb ALMA 1	18:29:05.55	+00:30:35.14	?	?	5

^a Position of the continuum peak in the 252 GHz datasets.

^b References. (1) Strom & Strom (1993) (2) Furlan et al. (2016) (3) Tobin et al. (2016) scaled to a distance of 300 pc for Perseus (Ortiz-León et al. 2018a) (4) Enoch et al. (2009) scaled to a distance of 436 for Serpens (Ortiz-León et al. 2018b) (5) Martín-Doménech et al. (2021).

^c For both sources in the binary combined. Per-emb-17 is an unresolved binary in our observations, while we resolve the East and West component of Ser-emb-11.

^d Likely an underestimate, because the source is saturated in 70 μm Spitzer observations (Enoch et al. 2009).

ing chemical surveys of low-mass protostars often either focus only on O-COMs (e.g., Bouvier et al. 2022) or cover not enough transitions with different upper level energies to derive excitation temperatures (e.g., Yang et al. 2021).

Therefore, in order to understand the conditions present during the initial stages of terrestrial-planet formation, we set out to search for hot gas around low-mass protostars and characterize its chemistry. We conducted the NOEMA program CATS-N-DOGS (Chemistry And Temperature: searching with NOEMA for Destruction of carbon GrainS) consisting of $0''.5\text{--}1''.5$ resolution observations of nine low-mass and one intermediate-mass protostar, covering ~ 16 GHz of bandwidth at 2 MHz resolution at 1, 2 and 3 mm. Here we present the results for the simplest O-COM (methanol; CH_3OH) and N-COM (methyl cyanide; CH_3CN), showing that hot ($\gtrsim 300$ K) gas is present toward all sources in our sample and that CH_3CN traces hotter gas than CH_3OH .

The paper is structured as follows. The targets and observations are described in Section 2. The results for CH_3CN and CH_3OH are presented in Sections 3.1–3.2 and 3.3, respectively, and the implications of these results are discussed in Section 4. Finally, the main conclusions are summarized in Section 5.

2. OBSERVATIONS AND METHODS

2.1. Source sample

We target low-mass protostars known to display CH_3OH emission (Hsieh et al. 2019; Bergner et al. 2019),

Table 2. Overview of observations.

Sources	1 mm (CH ₃ CN $J = 14 - 13$)			2 mm (CH ₃ CN $J = 12 - 11$)			3 mm (CH ₃ CN $J = 5 - 4$)		
	$I_{\text{peak}}(\text{cont})^a$ (K)	beam (arcsec)	line rms ^b (K)	$I_{\text{peak}}(\text{cont})^a$ (K)	beam (arcsec)	line rms ^b (K)	$I_{\text{peak}}(\text{cont})^a$ (K)	beam (arcsec)	line rms ^c (K)
HBC494	7.92 ± 0.01	0.98×0.32	0.25	1.288 ± 0.001	2.58×0.88	0.14
HOPS-370	1.30 ± 0.01	3.37×0.60	0.02	1.020 ± 0.010	4.18×0.48	0.04
Per-emb-17	3.54 ± 0.01	0.50×0.34	0.26	1.057 ± 0.003	1.30×0.42	0.18	0.370 ± 0.002	1.33×1.09	0.19
Per-emb-20	0.36 ± 0.05	0.49×0.34	0.18	0.092 ± 0.003	1.39×0.43	0.18	0.055 ± 0.001	1.29×1.04	0.19
Ser-emb-1	8.74 ± 0.01	0.76×0.32	0.19	2.222 ± 0.009	1.72×0.70	0.17	0.896 ± 0.002	2.32×0.83	0.13
Ser-emb-8	3.44 ± 0.02	0.75×0.32	0.20	1.084 ± 0.006	1.71×0.71	0.17	0.416 ± 0.002	2.29×0.84	0.13
Ser-emb-11E ^d	0.30 ± 0.01	0.77×0.33	0.19	0.110 ± 0.006	1.81×0.70	0.16	0.200 ± 0.002	2.33×0.83	0.13
Ser-emb-11W ^d	1.17 ± 0.01	0.77×0.33	0.19	0.338 ± 0.006	1.81×0.70	0.16	0.192 ± 0.002	2.33×0.83	0.13
Ser-emb-17 ^d	5.44 ± 0.01	0.77×0.33	0.19	1.552 ± 0.006	1.81×0.70	0.16	0.352 ± 0.002	2.33×0.83	0.13
Ser-emb ALMA 1 ^d	0.15 ± 0.01	0.77×0.33	0.19	0.052 ± 0.006	1.81×0.70	0.16	0.064 ± 0.002	2.33×0.83	0.13

Notes. Three dots (...) indicate that a particular setting has not been observed.

^a Continuum peak flux in the side band containing the CH₃CN transition. The central frequencies of these side bands are 89 GHz, 222 GHz and 260 GHz.

^b In 2 MHz channels (2.3–2.7 km s⁻¹).

^c In 2 km s⁻¹ channels.

^d Present in the same field of view.

but are not part of the MPG-IRAM Observatory Programs (MIOP)¹: Per-emb-17, Per-emb-20, Ser-emb-1, Ser-emb-8 (also known as S68N) and Ser-emb-17. The field of view of Ser-emb-17 contains the protostellar binary Ser-emb-11 and the protostar Ser-emb ALMA 1 (Martín-Doménech et al. 2021). The sources in Ser-emb-11 are separated by $\sim 2''$, and only the western source displays emission from complex organics (Martín-Doménech et al. 2021). The same work detected only one weak low-excitation (50 K) CH₃OH transition toward Ser-emb ALMA 1 and therefore concluded that the source most likely does not harbor a hot corino. Per-emb-17 is a close binary ($0''.28$; Tobin et al. 2016), which we do not resolve. The luminosities for these sources range between 2.4–7.1 L_{\odot} (Table 1). In addition we targeted the FU-Ori type protostar HBC494 (also known as Reipurth 50 N IRS 1; Reipurth & Bally 1986) with a luminosity of $\sim 300 L_{\odot}$ (Strom & Strom 1993), as this type of luminous sources can display line-rich spectra (e.g., van 't Hoff et al. 2018; Lee et al. 2019). We also observe the intermediate-mass protostar HOPS-370 (314 L_{\odot}) also known as OMC2-FIR3 (Chini et al. 1997) and VLA 11 (Reipurth et al. 1999), for which a protostellar disk and CH₃OH have been detected (Tobin et al. 2019, 2020). With its higher luminosity and hence warmer circumstellar material, HOPS-370 may serve as a template for what hot-gas emission could look like. Both HBC494 and HOPS-370 are located in the Orion molecular cloud. Source properties are listed in Table 1.

2.2. Observations

For all sources, except HBC494 and HOPS-370, we observe CH₃CN $J_K = 5_K - 4_K$ (91 GHz), $J_K = 12_K - 11_K$ (220 GHz) and $J_K = 14_K - 13_K$ (257 GHz). $J_K = 5_K - 4_K$ is not observed toward HOPS-370 and $J_K = 12_K - 11_K$ is not observed toward HBC494. All three settings cover a suite of CH₃OH transitions. The entire dataset is obtained through five different IRAM-NOEMA programs and an observing log is presented in Table A1. All observations are carried out between February 2020 and November 2021 in A configuration, except for the 220 GHz observations toward the Serpens sources, which are obtained with the more compact C configuration. The HOPS-370 257 GHz observations are taken in both A and C configuration. The PolyFiX correlator provides ~ 16 GHz of bandwidth, divided over two ~ 8 GHz sidebands, at 2 MHz resolution. In addition, several narrow, 62.5 kHz resolution spectral windows are placed within the sidebands. Our 1 mm setting covers the frequency ranges of 240.9–248.6 GHz and 256.4–264.1 GHz, the 2 mm setting covers the frequency ranges of 202.7–210.8 GHz and 218.2–226.3 GHz, and the 3 mm setting covers the frequency ranges of 85.2–93.3 GHz and 100.7–108.8 GHz. Here we focus on the 2 MHz resolution spectra, except for CH₃CN $5_K - 4_K$, for which we use a high spectral resolution window between 91.92–92.01 GHz binned to 2 km s⁻¹ to obtain a velocity resolution comparable to that of the $12_K - 11_K$ and $14_K - 13_K$ transitions.

¹ <https://iram-institute.org/science-portal/proposals/lp/miop/>

The data are calibrated using the CLIC package of the GILDAS² software, using the most recent GILDAS version available at the time of data reduction (July after a dataset was observed, i.e., 2020 or 2021). The imaging and cleaning was done using the MAPPING package of GILDAS. Self-calibration was performed on the continuum, except for Per-emb-20 for which the continuum is too weak and for HOPS-370 for which the spectrum is too line rich to isolate enough line free channels. The self-calibration solutions were transferred to the spectral line cubes, which were then continuum subtracted and cleaned. The resulting beam sizes and rms are listed in Table 2. Finally, we extracted spectra toward the continuum peak pixel using the CLASS package of GILDAS.

For HOPS-370, we imaged the data without continuum subtraction and applied a statistical method as for example used by Jørgensen et al. (2016) for the line-rich spectrum of the protostellar binary IRAS 16293, to subtract the continuum from the spectra. This method entails the formation of a density distribution of flux values in the spectrum. If there would only be continuum emission, the density distribution would represent a symmetric Gaussian centered at the continuum level. In the case of continuum and line emission, the Gaussian will contain an exponential tail toward higher values. The continuum level can then be determined by fitting a skewed Gaussian to the distribution. Given the large bandwidth of the NOEMA observations, we fit the density distribution per 1/8 of the bandwidth of each baseband (~ 1 GHz regions). The combination of high line density and intermediate spectral resolution results in double peaked distributions at 2 mm, where we take the peak at the lowest intensity as the continuum level. The line density is even higher at 1 mm, and the peak overpredicts the continuum level as it is located at intensity values $\gtrsim 7\sigma$. We therefore estimate the continuum level as the intensity 3σ above the intensity of the lowest bin. We then fit a first-order polynomial to the eight measurements for each baseband to take into account the continuum spectral index, and subtract this from the spectrum. The resulting spectra around the CH₃CN $J = 14 - 13$ and $J = 12 - 11$ ladders are displayed in Fig. 1.

2.3. Rotation diagram analysis

A rotation diagram analysis is a commonly used technique to derive column densities and excitation temperatures from molecular line emission (e.g., Goldsmith & Langer 1999). In local thermodynamic equilibrium

(LTE), the column density, N , and rotational temperature, T_{rot} , can be calculated using the relation

$$\frac{N_{\text{up}}}{g_{\text{up}}} = \frac{N}{Q(T_{\text{rot}})} e^{(-E_{\text{up}}/T_{\text{rot}})}, \quad (1)$$

where g_{up} is the upper level degeneracy, E_{up} is the upper level energy, and Q is the molecular partition function. N_{up} is the column density of the upper level, which can be determined from the observed line flux, $W = \int T_{\text{mb}} dv$, assuming the emission is optically thin, using

$$N_{\text{up}} = \frac{8\pi k\nu^2 W}{hc^3 A_{ul}}, \quad (2)$$

where A_{ul} is the Einstein A coefficient and ν the frequency of the transition. The column density and rotational temperature can then be derived from the intercept and slope, respectively, of a linear fit to $\log(N_{\text{up}}/g_{\text{up}})$ versus E_{up} .

When the emission is not optically thin, an optical depth correction factor, $C_\tau = \tau/(1 - e^{-\tau})$, must be applied to derive the true level populations:

$$N_{\text{up}} = N_{\text{up}}^{\text{obs}} C_\tau, \quad (3)$$

where the optical depth, τ , depends on the upper level column density via

$$\tau = \frac{c^3 A_{ul} N_{\text{up}}}{8\pi\nu^3 \Delta\nu} (e^{h\nu/kT_{\text{rot}}} - 1), \quad (4)$$

where $\Delta\nu$ is the full width at half maximum (FWHM) of the line.

Even though some CH₃CN transitions appear optically thick in the rotation diagram, as will be described in Sect. 3.1.1, the observed line fluxes cannot be reproduced with optically thick emission under the assumption that the unresolved emission fills the beam. Taquet et al. (2015) dealt with this by running a large grid of models with varying rotational temperature, column density and source size. On the other hand, Bergner et al. (2019) introduced a beam dilution factor to Eq. 3, based on an educated estimate of the emitting area, Ω_s , such that

$$N_{\text{up}} = N_{\text{up}}^{\text{obs}} C_\tau \frac{\Omega_b}{\Omega_s}, \quad (5)$$

where Ω_b is the solid angles of the beam. The beam and source solid angles can be expressed as $\Omega_b = \theta_{\text{maj}}\theta_{\text{min}}$ and $\Omega_s = \theta_s^2$, respectively, where θ_{maj} and θ_{min} are the major and minor axis of the beam, and θ_s is the emitting radius. Synthetic upper level populations with the total column density and rotational temperature as free parameters can then be generated by substituting Eqs. 4 and 5 into Eq. 1, and they are then fitted to the observed

² <https://www.iram.fr/IRAMFR/GILDAS/>

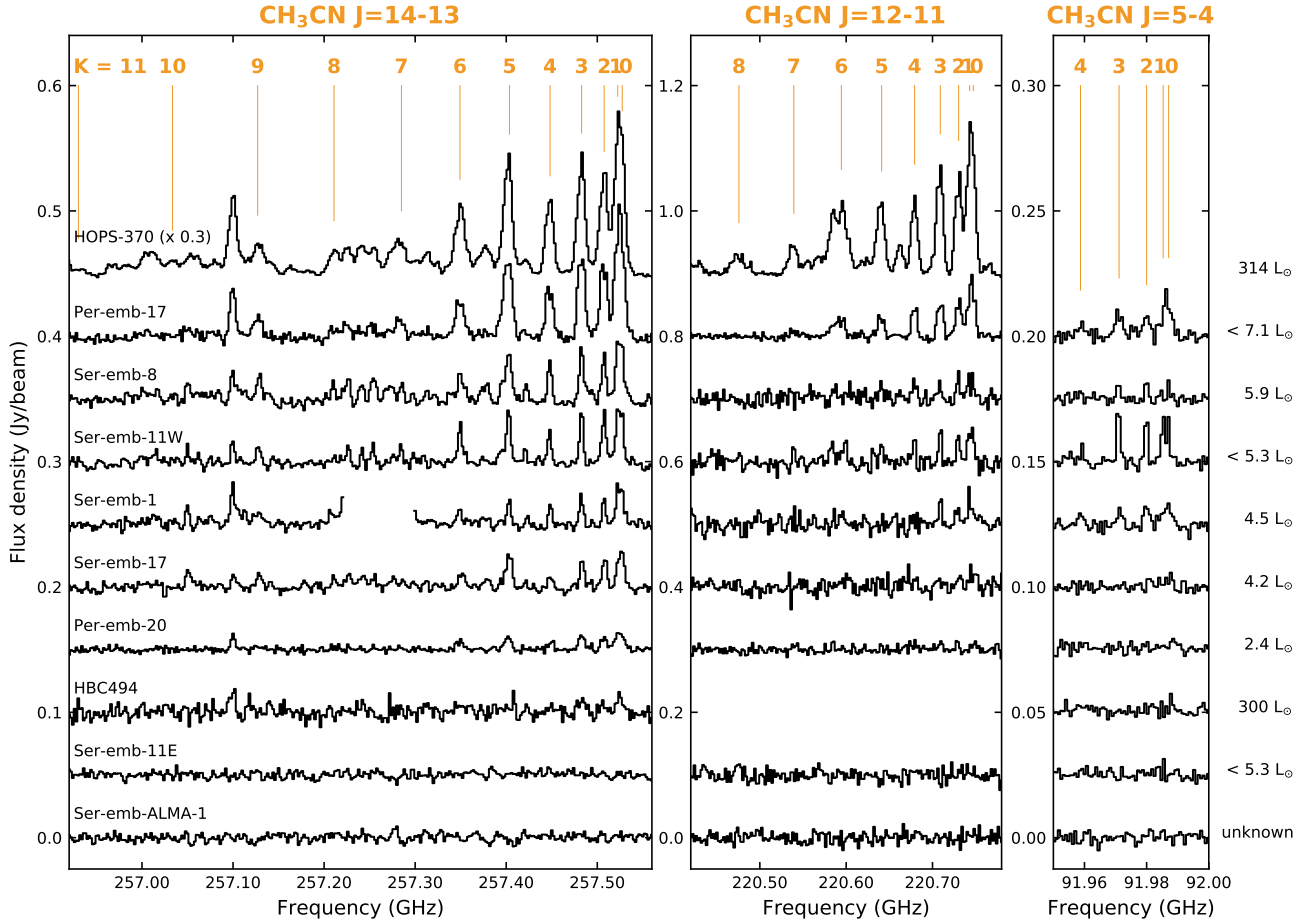


Figure 1. Overview of CH₃CN $J_K = 14_K - 13_K$ (left panel), $J_K = 12_K - 11_K$ (middle panel), and $J_K = 5_K - 4_K$ (right panel) spectra at ~ 2 km s⁻¹ resolution extracted toward the continuum peak for the sources in our sample. The vertical orange lines mark the different K -components in each ladder. Ser-emb-1 displays strong emission from ²⁹SiO $J = 6 - 5$ at 257.255202 GHz, and this region of the spectrum is omitted. The $14_5 - 13_5$ transition is blended with a CH₃OH line. The vertical scale is the same for all sources, except the $14_K - 13_K$ spectrum towards HOPS-370 is scaled by a factor 0.3, but varies for the three different J -transitions. Bolometric luminosities are listed on the right, where a < sign is used for binaries where the luminosity only has been measured for both components combined.

level populations (Eq. 1) using the Markov Chain Monte Carlo (MCMC) package emcee (Foreman-Mackey et al. 2013) to sample the posterior distribution (e.g., Loomis et al. 2018). Since we here want to investigate whether CH₃CN and CH₃OH have similar or different emitting areas toward eight different sources, we adopt the computationally more effective approach by Bergner et al. (2019), but add the source solid angle as free parameter. Following Goldsmith & Langer (1999) and Taquet et al. (2015), we will use the term “population diagram” when corrections are applied for emitting area and optical depth and “rotation diagram” when these corrections are not made. Details about the line flux measurements and spectroscopic data are provided in Appendix B.

Yang et al. (2021) concluded that LTE is a valid assumption for 1 mm CH₃OH emission toward the Perseus protostars in the PEACHES sample. Per-emb-20 is

among the PEACHES sources with the lowest estimated gas densities ($\sim 3 \times 10^9$ cm⁻³) based on the continuum flux, and by far the weakest continuum source in our sample. LTE is also a good assumption for CH₃CN as the critical densities of the transitions are a few times 10^6 cm⁻³ for $14_K - 13_K$ up to a few times 10^7 cm⁻³ for $5_K - 4_K$ based on RADEX calculations (see also Shirley 2015, Walls et al., under review).

3. RESULTS AND ANALYSIS

3.1. CH₃CN

An overview of all CH₃CN observations is shown in Fig. 1. $J_K = 14_K - 13_K$ transitions are detected toward all sources except Ser-emb-11E and Ser-emb-ALMA-1. These latter two sources display very line-poor spectra and we exclude them from further analysis here. The $14_K - 13_K$ lines are strongest toward the intermedi-

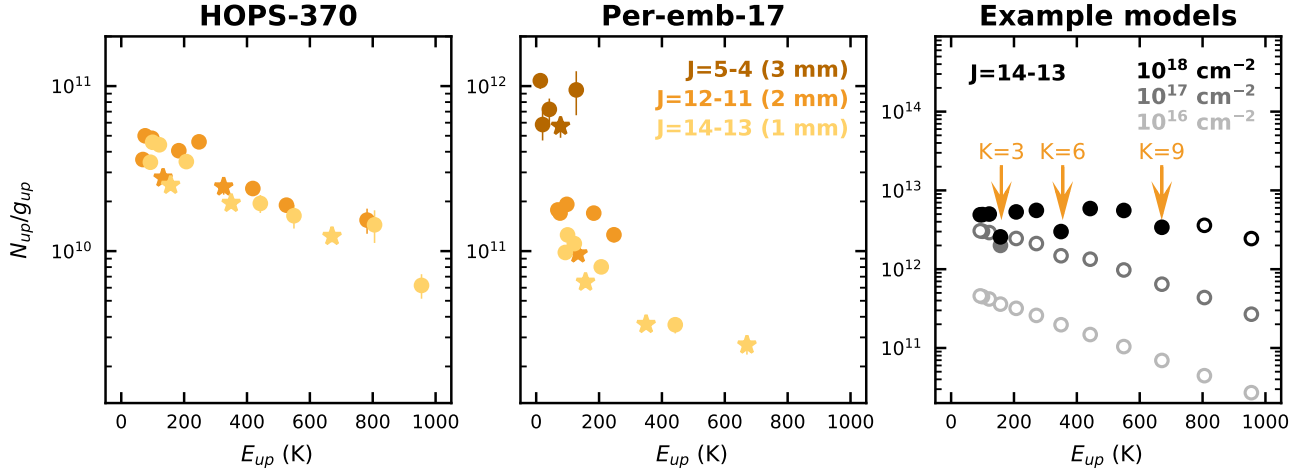


Figure 2. Rotation diagrams for the CH_3CN $J = 5 - 4$ (dark orange), $J = 12 - 11$ (orange), and $J = 14 - 13$ (yellow) ladders toward HOPS-370 and Per-emb-17. $K = 3$, $K = 6$ and $K = 9$ transitions are shown as star symbols, the other transitions are shown as circles. The unresolved $12_K - 11_K$ and $5_K - 4_K$ fluxes have been scaled to the smaller beam size of the unresolved $14_K - 13_K$ observations. The error bars correspond to 1σ , and are typically smaller than the symbols. Rotation diagrams for the other sources in the sample are shown in Fig. C1. The right panel displays three LTE models for the $J = 14 - 13$ ladder at 300 K with varying column densities (different shades of gray), highlighting the behavior of the $K = 3$, $K = 6$ and $K = 9$ transitions when the emission becomes optically thick. Optically thin transitions in this panel are shown as open symbols, and optically thick transitions as filled symbols.

ate mass source HOPS-370, where K -components up to $K = 11$ are detected. The brightest low-mass source is Per-emb-17, and all low-mass sources except Per-emb-20 and HBC494 display emission up to $14_9 - 13_9$. For Per-emb-20, the highest detected transition is $14_6 - 13_6$, and despite its high luminosity of $\sim 300 L_\odot$, only $K = 0 - 4$ are weakly detected toward HBC494. HBC494 has the strongest continuum peak in the sample after HOPS-370 (Table 2), so the line-poor spectrum is not due to a low mass of the circumstellar material, but may be related to the continuum optical depth. With the exception of HBC494, there seems to be a rough trend between line strength and bolometric luminosity, although the luminosities for Per-emb-17, Ser-emb-11E and Ser-emb-11W are the luminosities for both binary components combined.

The $12_K - 11_K$ transitions are only detected toward HOPS-370, Per-emb-17, Ser-emb-1, Ser-emb-8 and Ser-emb-11W. This can be attributed to both the $12_K - 11_K$ transitions being intrinsically weaker than the $14_K - 13_K$ transitions under given conditions, as well as the lower sensitivity of the $12_K - 11_K$ observations. For HOPS-370, transitions up to $12_{10} - 11_{10}$ are detected. For the brightest low-mass source the highest transition detected is $12_7 - 11_7$ (Ser-emb-11W), but the strong $12_9 - 11_9$ line is blended with ^{13}CO .

The $5_K - 4_K$ transitions are much weaker than transitions from the other two ladders and are detected toward Per-emb-17, Ser-emb-1, Ser-emb-8, and Ser-emb-11W. The emission is particularly strong toward Ser-

emb-11W. Except for Ser-emb-8, all K -components are detected. Only Ser-emb-8 shows signs of large scale emission being resolved out, especially for $5_0 - 4_0$ and $5_1 - 4_1$, as evidenced by large scale ripples with deep negative bowls in the velocity channels.

3.1.1. Rotation diagrams

Rotation diagrams including all detected CH_3CN transitions toward HOPS-370 and Per-emb-17 are presented in Fig. 2 and toward the other sources in Fig. C1. The beam size of the observations increases with wavelength, but even in the smallest beam of the 1 mm observations ($J = 14 - 13$) all emission is unresolved. Given the similar upper-level energies, we assume that the emission at 2 and 3 mm is also originating in a region smaller than the 1 mm beam. We therefore correct for the additional dilution within the larger beams at 2 and 3 mm by scaling the integrated intensities (in units of K km s^{-1}) at 2 and 3 mm by $\theta_x^2/\theta_{1\text{mm}}^2$, where θ_x is the beam size at 2 or 3 mm.

For optically thin emission, all transitions lie on a straight line with a negative slope. Because the $K = 3, 6, 9$ transitions have double the statistical weight compared to the other K -transitions of a specific ladder but similar Einstein A coefficients, they can become optically thick while the other transitions remain optically thin. In this case, the optically thick line is weaker than expected for optically thin emission, which will result in the optically thick transition to end up below the linear trend in the rotation diagram (see Fig. 2, right panel).

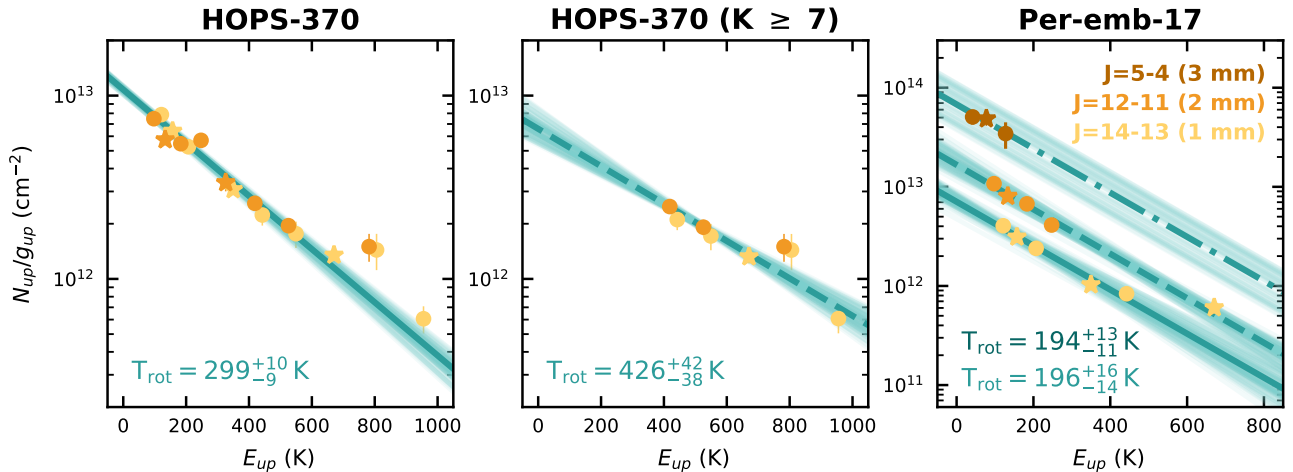


Figure 3. Population diagram analysis for CH_3CN emission toward HOPS-370 and Per-emb-17. $K = 3$, $K = 6$ and $K = 9$ transitions are shown as star symbols, the other transitions are shown as circles. The error bars correspond to 1σ , and are typically smaller than the symbols. For HOPS-370, the $J = 12 - 11$ (orange), and $J = 14 - 13$ (yellow) ladders are modeled together. In the left panel all transitions are included, while the middle panel shows the result for the optically thin transitions with $K \geq 7$. For Per-emb-17, the $J = 5 - 4$ (dark orange), $J = 12 - 11$ (orange), and $J = 14 - 13$ (yellow) ladders are modeled individually (right panel). Draws from the fit posteriors are shown with light teal lines, with the 50th percentiles shown as thick teal lines. The corresponding rotational temperature is listed in the bottom left corner. For Per-emb-17, the top temperature is from the $J = 12 - 11$ fit, the bottom from the $J = 14 - 13$ fit. A solid line indicates that the rotational temperature, column density and source size were fitted, a dashed line indicates that the source size was fixed and a dash-dotted line indicates that the rotational temperature was fixed (see Table 3 for details and all fit results). Population diagrams for the other sources in the sample are shown in Figs. C2- C4.

If the column is high enough for all K -components to be optically thick, they will form a straight line with a slight positive slope with the $K = 3, 6, 9$ transitions below the trend (see Fig. 2, right panel). Finally, for optically thick emission, the $12_K - 11_K$ transitions will be located slightly above the $14_K - 13_K$ transitions, and the $5_K - 4_K$ transitions will be even higher up for a given column density and temperature.

With the above in mind, it is clear from Figs. 2 and C1 that the $J = 14 - 13$ ladder is only fully optically thin toward HBC494. For all other sources, at least the $14_3 - 13_3$ transition is optically thick. For Ser-emb-1, Ser-emb-8 and Ser-emb-17, the $K = 7 - 9$ transitions appear overly strong compared to the lower K -transitions, suggesting that there may be two temperature components.

The $J = 12 - 11$ ladder is detected toward five of the eight sources in the sample (Fig. C1), but only for HOPS-370 are the $14_K - 13_K$ and $12_K - 11_K$ transitions showing the same behavior. For the other sources with detections, the $12_K - 11_K$ transitions are typically higher up in the rotation diagram than $14_K - 13_K$ transitions with similar E_{up} . This suggests that they are either (more) optically thick, and/or trace a larger column of material than $14_K - 13_K$.

Ser-emb-1 is the only source where the $12_K - 11_K$ transitions appear optically thin, although it is diffi-

cult to determine with no detections of $14_4 - 13_4$ and $14_5 - 13_5$ and a tentative detection of $14_6 - 13_6$. For Per-emb-17, Ser-emb-8 and Ser-emb-11W, all observed $12_K - 11_K$ transitions appear at least marginally optically thick with $12_3 - 11_3$ and $12_6 - 11_6$ (if detected) clearly below the linear trend of the entire ladder and a nearly horizontal slope. The $12_K - 11_K$ transitions thus appear more optically thick than the $14_K - 13_K$ transitions toward these three sources.

The $5_K - 4_K$ transitions are located above the $12_K - 11_K$ and $14_K - 13_K$ transitions in the rotation diagram for all sources with detections (Figs. 2 and C1). Again, suggesting that they are either optically thick, and/or trace a larger column of material. While the $K = 0 - 2$ components get optically thick at low temperatures ($\lesssim 30$ K) for column densities a few times 10^{15} cm^{-2} , the $K = 3$ and $K = 4$ components become most easily optically thick at temperatures of $30 - 40$ K, which then requires column densities of $\sim 10^{16} \text{ cm}^{-2}$ and $\sim 10^{17} \text{ cm}^{-2}$, resp (Fig. D1). In addition, for the $5_4 - 4_4$ transition to become half the strength of the $5_2 - 4_2$ transition (as observed; Fig. 1), column densities $\gtrsim 10^{17} \text{ cm}^{-2}$ are required (Fig. D1). Such high columns of cold material are unlikely as CH_3CN column densities of a few times $10^{11} - 10^{12} \text{ cm}^{-2}$ are reported toward dark clouds and prestellar cores (Minh et al. 1993; Vastel et al. 2019; Megias et al. 2023). This suggests that the observed

Table 3. Rotational temperatures, column densities and source sizes for CH₃CN.

Source	$J = 14 - 13$ (1 mm)			$J = 12 - 11$ (2 mm)			$J = 5 - 4$ (3 mm)		
	T_{ex} (K)	N (cm ⁻²)	θ_s (arcsec)	T_{ex} (K)	N (cm ⁻²)	θ_s (arcsec)	T_{ex} (K)	N (cm ⁻²)	θ_s (arcsec)
HBC494	$\lesssim 388$	$\lesssim 4.0 \times 10^{15}$	[0.122] ^a	[388]	$< 1.1 \times 10^{17}$	[0.122] ^a
HOPS-370	278^{+14}_{-13}	$(1.4^{+0.3}_{-0.3}) \times 10^{17}$	$0.151^{+0.004}_{-0.004}$	273^{+19}_{-17}	$(1.9^{+0.4}_{-0.4}) \times 10^{17}$	$0.132^{+0.003}_{-0.003}$
Per-emb-17	195^{+15}_{-14}	$(4.4^{+1.1}_{-1.0}) \times 10^{16}$	$0.089^{+0.003}_{-0.003}$	194^{+13}_{-11}	$(1.0^{+0.2}_{-0.2}) \times 10^{17}$	[0.089]	[195]	$(4.2^{+1.7}_{-1.4}) \times 10^{17}$	$0.080^{+0.006}_{-0.005}$
Per-emb-20	343^{+99}_{-93}	$(1.1^{+1.3}_{-0.7}) \times 10^{17}$	$0.030^{+0.006}_{-0.004}$	[343]	$< 9.7 \times 10^{16}$	[0.030]	[343]	$< 1.0 \times 10^{18}$	[0.030]
Ser-emb-1	388^{+75}_{-86}	$(2.1^{+1.5}_{-1.1}) \times 10^{17}$	$0.034^{+0.005}_{-0.003}$	—	—	—	[388]	$(4.2^{+2.3}_{-1.7}) \times 10^{18}$	$0.050^{+0.004}_{-0.003}$
Ser-emb-8	358^{+54}_{-46}	$(1.6^{+0.8}_{-0.5}) \times 10^{17}$	$0.049^{+0.004}_{-0.004}$	355^{+49}_{-41}	$(5.3^{+2.5}_{-2.0}) \times 10^{17}$	[0.049]	[358]	$(2.4^{+0.8}_{-0.9}) \times 10^{18}$	[0.049]
Ser-emb-11W	309^{+49}_{-41}	$(7.5^{+3.3}_{-2.4}) \times 10^{16}$	$0.056^{+0.004}_{-0.004}$	343^{+33}_{-31}	$(4.4^{+1.1}_{-0.9}) \times 10^{17}$	[0.056]	[309]	$(1.8^{+1.2}_{-0.7}) \times 10^{17}$	$0.15^{+0.03}_{-0.02}$
Ser-emb-17	347^{+59}_{-79}	$(1.5^{+1.4}_{-0.8}) \times 10^{17}$	$0.033^{+0.006}_{-0.004}$	[347]	$< 1.3 \times 10^{17}$	[0.033]	[347]	$< 6.9 \times 10^{17}$	[0.033]

Notes. Rotational temperature, column density and source size determined from population diagram analysis. Listed values and uncertainties correspond to the 50th, and 16th and 84th percentiles, respectively, of the posterior distributions. For the column densities, a flux calibration uncertainty (20% at 1 and 2 mm, 10% at 3 mm) has been added to the fit uncertainty through a root sum square. For sources with no $5_K - 4_K$ and/or $12_K - 11_K$ detections upper limits are calculated using the rotational temperature and source size derived from the $14_K - 13_K$ transitions. Values listed between square brackets are kept fixed at the value derived from the $14_K - 13_K$ transitions, unless noted otherwise. Three dots (...) indicate that a frequency range has not been observed, and a dash (—) indicates that not enough transitions have been detected at high enough signal to noise to obtain a reliable fit. For HOPS-370, the combined fit to the $14_K - 13_K$ and $12_K - 11_K$ transitions combined results in 299 ± 10 K and $(1.6 \pm 0.3) \times 10^{17}$ cm⁻².

^a Source size kept fixed at the deconvolved continuum size.

$5_K - 4_K$ emission is not simply tracing optically thick cold emission from the outer envelope. Instead, the $5_K - 4_K$ transitions at 90 GHz are likely to trace a larger column of material than the $14_K - 13_K$ and $12_K - 11_K$ transitions because of the lower dust opacity at these longer wavelengths (3 mm).

3.1.2. Population diagram analysis

Due to the combination of optically thin and thick lines, we can constrain the rotational temperature, column density and emitting area from the $14_K - 13_K$ transitions as described in Sect. 2.3. Since the $14_0 - 13_0$ and $14_1 - 13_1$ transitions are blended we exclude them from the population diagram analysis. The population diagrams for HOPS-370 and Per-emb-17 are presented in Fig. 3, and for the other sources in Fig. C2. The best fit parameters, defined as the 50th percentile of the posterior distributions, are listed in Table 3.

The derived rotational temperatures from the $14_K - 13_K$ transition range between 195–390 K (see also Fig. 4). While reasonable fits can be obtained to all $14_K - 13_K$ transitions for most sources, the highest K -transitions toward HOPS-370 and Per-emb-17 can not be reproduced with a single temperature component. For HOPS-370, the transitions with $K > 6$ are optically thin ($\tau < 0.35$). Fitting these transitions separately (with a fixed source size) results in a rotational temperature of 426^{+42}_{-38} K (Fig. 3). For Per-emb-17, fewer high K transitions are detected and $14_6 - 13_6$ is marginally optically thick ($\tau = 0.6$). The rotational temperature from a fit to the high K transitions alone is therefore not well constrained, but suggests $T_{\text{rot}} \gtrsim 400$ K. For Ser-emb-1,

Ser-emb8, and Ser-emb-17, there seems to be a change in slope of the population diagram for $K > 6$, but given the small number of transitions and the emission being unresolved, fits to the high K components are not well constrained.

As expected from the rotation diagrams (Sect. 3.1.1), only for HOPS-370 can the $14_K - 13_K$ and $12_K - 11_K$ transitions be reproduced by a single model. We therefore analyze the $12_K - 11_K$ transitions separately. However, with fewer lines detected than for the $J = 14 - 13$ ladder and potentially fully optically thick emission, we cannot constrain the rotational temperature, column density and source size simultaneously from the $J = 12 - 11$ ladder. We therefore fix the source size to that derived from the $14_K - 13_K$ transitions. The resulting population diagram for Per-emb-17 is presented in Fig. 3, and for the other sources in Fig. C3. All fit parameters are listed in Table 3.

While the resulting rotational temperatures are similar to the ones derived from the $14_K - 13_K$ transitions, the column densities are a factor of a few higher. Probing higher column densities at 2 mm could either be a reflection of the $12_K - 11_K$ transitions becoming optically thick at slightly higher columns than the $14_K - 13_K$ transitions due to lower Einstein A coefficients, or because the dust opacity is slightly lower at 2 mm compared to 1 mm allowing more material to be observed. The more optically thick nature of the $12_K - 11_K$ transitions in the rotation diagram, as particularly evident for Ser-emb-11W, favors the latter explanation.

The $J = 5 - 4$ ladder only has three unblended transitions ($K = 2 - 4$) so we cannot constrain rotational

temperature, column density and source size simultaneously. We fix the rotational temperature to the value derived from the $14_K - 13_K$ transitions, because the rotational temperature cannot be constrained without knowledge of the emitting area for optically thick emission, and if we are indeed tracing more material at 3 mm due to the lower dust opacity, the emitting areas at 1 and 3 mm will not be the same. The resulting population diagram for Per-emb-17 is presented in Fig. 3, and for the other sources in Fig. C4. All fit parameters are listed in Table 3. For the sources with a detection of the $5_K - 4_K$ transitions, the column density is a factor 8–46 higher than derived from the $14_K - 13_K$ transitions when scaling to the same emitting area (Fig. 5). The smallest increase is derived for Per-emb-17 and the largest increase toward Ser-emb-1. The upper limits based on the $5_K - 4_K$ nondetections toward HBC494, Per-emb-20 and Ser-emb-17 are consistent with column density increases at 3 mm up to a factor 27, 8.9 and 4.7, respectively. The derived emitting area at 3 mm is only a factor 1.5 and 2.7 larger for Ser-emb-1 and Ser-emb-11W, respectively, while it is a factor 0.9 smaller for Per-emb-17. The source size was fixed in the fit for Ser-emb-8 because the $5_4 - 4_4$ transition was not detected. The increases in column density at 3 mm are thus not due to a smaller emitting area retrieved from the fit. Instead, the larger column densities and emitting areas suggest that we see more material closer to the star at 3 mm than at 1 mm.

Overall, the CH_3CN emission shows rotational temperatures higher than ~ 300 K, based on the $J = 14 - 13$ ladder. In addition, we may be probing larger columns with the $5_K - 4_K$ transitions at 90 GHz, and maybe already with the $12_K - 11_K$ transitions at 220 GHz, which would be consistent with lower dust opacities at lower frequencies.

3.2. $\text{CH}_3^{13}\text{CN}$

The $\text{CH}_3^{13}\text{CN}$ transitions are located close to the corresponding main isotopologue transitions in frequency space. We do not detect $\text{CH}_3^{13}\text{CN}$ toward any of the sources in the sample, but we are able to put constraints on the excitation temperature of a potentially second temperature component for Ser-emb-1, Ser-emb-8 and Ser-emb-17 using the non-detection of $\text{CH}_3^{13}\text{CN}$ $J_K = 14_K - 13_K$. For increasing temperatures, the $\text{CH}_3^{13}\text{CN}$ column density upper limit derived from the 3σ noise level increases, while at the same time a lower column is required to reproduce the high- K transitions of CH_3CN . This means that the combination of observational constraints places a lower limit on the excitation temperature, as for too low temperatures the column

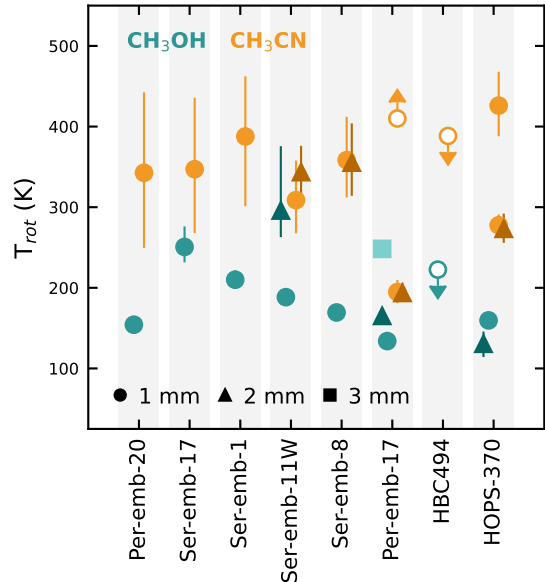


Figure 4. Overview of rotational temperatures derived for CH_3CN (orange) and CH_3OH (teal), with sources ordered by their bolometric luminosity. Temperatures derived from the 1 mm data ($J_K = 14_K - 13_K$ for CH_3CN) are shown as circles, from the 2 mm data ($J_K = 12_K - 11_K$ for CH_3CN) as triangles, and from the 3 mm data as squares. The highest orange circles for Per-emb-17 and HOPS-370 are derived from the high- K transitions only. Upper and lower limits are indicated with open symbols with an arrow pointing up or down, respectively.

density needed to explain the high- K CH_3CN emission should have resulted in a detection of $\text{CH}_3^{13}\text{CN}$.

Our approach is as follows. We model the $14_6 - 13_6$ to $14_9 - 13_9$ transitions using a fixed temperature. Using this temperature and the best fit column density (or the lowest column that results in optically thick emission), we calculate the expected $\text{CH}_3^{13}\text{CN}$ column assuming a $^{12}\text{C}/^{13}\text{C}$ ratio of 68 (Milam et al. 2005). If the expected $\text{CH}_3^{13}\text{CN}$ column exceeds the derived upper limit, this process is repeated with a 10 K higher excitation temperature. To be in agreement with the $\text{CH}_3^{13}\text{CN}$ non-detection, the excitation temperatures then need to be $\gtrsim 250$, $\gtrsim 300$, and $\gtrsim 290$ K, respectively, for Ser-emb-1, Ser-emb-8 and Ser-emb-17. This confirms the presence of ~ 300 K gas toward these sources.

3.3. CH_3OH

The 1 mm setting covers the most CH_3OH transitions, and for all sources except HBC494, transitions with upper level energies ranging between ~ 30 and ~ 600 K are detected (Fig. 6 and Table B3). The highest upper level energy detected toward HBC494 is 73 K, while toward HOPS-370, Per-emb-17, Ser-emb-8 and Ser-emb-11W transitions with upper level energies up to ~ 800 K

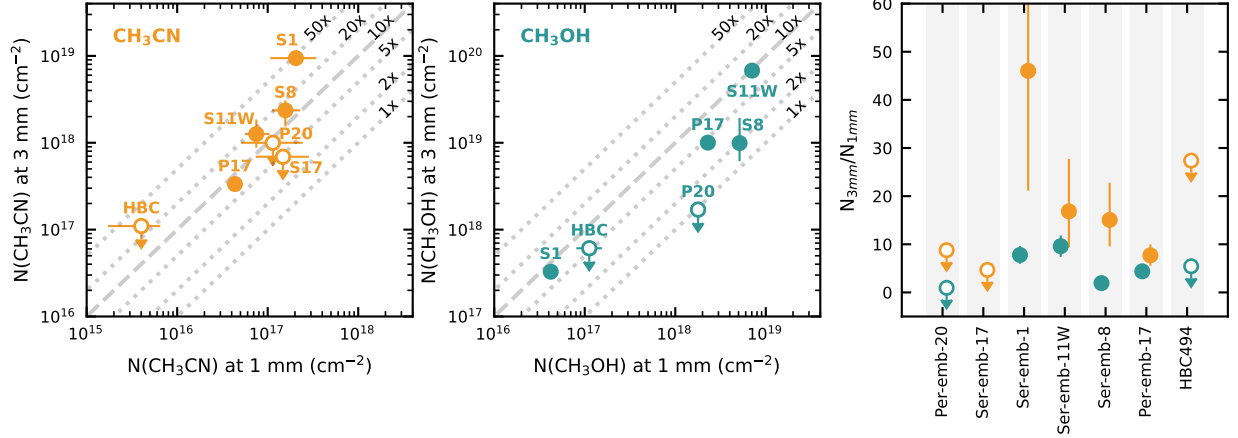


Figure 5. Comparison of column densities derived at 1 mm ($J_K = 14_K - 13_K$ for CH_3CN) and 3 mm ($J_K = 5_K - 4_K$ for CH_3CN). The left and middle panel show the 3 mm column versus the 1 mm column for CH_3CN and CH_3OH , respectively. Sources are identified by the first letter and the number in their names, except HBC494 which is abbreviated to HBC. The dotted and dashed gray lines mark increases in the 3 mm column of 1, 2, 5, 10 (dashed), 20 and 50 times compared to the 1 mm column, going from bottom right to top left. The right panel shows the ratio between the column density at 3 mm and 1 mm for CH_3CN (orange) and CH_3OH (teal) per source, with sources ordered by bolometric luminosity. For sources where a source size could be constrained for the 3 mm CH_3CN emission the column densities are scaled to the 1 mm source size. No 3 mm observations were performed toward HOPS-370. Upper and lower limits are indicated with open symbols with arrows.

are detected. The 2 mm setting covers the least CH_3OH transitions. The most lines are detected toward HOPS-370, Per-emb-17 and Ser-emb-11W, with upper level energies ranging between ~ 15 –600 K. No transitions are detected at 2 mm toward Ser-emb-1 and Ser-emb-8, and no 2 mm observations were carried out toward HBC494. The transitions detected in the 3 mm setting span a smaller range of upper level energies (~ 30 –330 K), but transitions with lower Einstein A coefficients are detected (down to $8 \times 10^{-7} \text{ s}^{-1}$ versus $1 \times 10^{-6} \text{ s}^{-1}$ at 1 mm). No transitions are detected at 3 mm toward HBC494 and Per-emb-20, and no 3 mm observations were carried out toward HOPS-370.

Rotation diagrams for CH_3OH are presented in Fig. 6 for Per-emb-17 and in Fig. C5 for all sources in the sample. Similar as seen for CH_3CN , transitions at longer wavelengths are typically located higher up in the rotation diagram. Results of the population diagram analysis are presented in Fig. 6 for Per-emb-17 and in Figs. C6–C8 for the other sources. All results are listed in Table 4. The 1 mm transitions are generally at least partially optically thick, except for Ser-emb-1 where the emission appears optically thin. The derived rotational temperatures at 1 mm range between $134 \pm 1 \text{ K}$ (Per-emb-17) and $251_{-19}^{+25} \text{ K}$ (Ser-emb-17) (see also Fig. 4). In contrast to CH_3CN , there is no evidence for two temperature components. The rotational temperature derived for HBC494 has a large uncertainty because only a few low-energy transitions are detected. The non-detection of the $17_{3,14} - 17_{2,15}$ transition at 248.282424 GHz ($E_{\text{up}} =$

405 K) provides the strongest constraint on the temperature and restricts it to values below $\sim 223 \text{ K}$.

For HOPS-370, the 1 and 2 mm data points are again in good agreement. For L1455-IRS1, the 2 mm data points are visibly higher up in the rotation diagram and a fit to the 2 mm data results in a slightly higher temperature ($165 \pm 6 \text{ K}$ versus $134 \pm 1 \text{ K}$), and a similar column density ($2.3 \pm 0.5 \times 10^{18} \text{ cm}^{-2}$ versus $2.2 \pm 0.5 \times 10^{18}$) for a larger emitting area (0.139 ± 0.006 versus 0.117 ± 0.001). Due to the low number of detections, excitation temperature, column density and source size cannot be constrained simultaneously for the other sources at 2 mm. For Ser-emb-11W, fixing the emitting area to that derived at 1 mm also results in a higher temperature and factor ~ 2 higher column density. For Per-emb-20 and Ser-emb-1, the 2 mm results are consistent with the conditions derived at 1 mm, while for Ser-emb-8 the upper limit is an order of magnitude lower than the 1 mm column density. For Ser-emb-17, the large scatter between the two detections does not allow for a firm conclusion to be drawn.

For Per-emb-17, Ser-emb-1 and Ser-emb-11W, the 3 mm data points are clearly higher up in the rotation diagram compared to the transitions at 1 and 2 mm. For Per-emb-17, the transitions appear optically thin ($\tau < 0.3$ for all but one transition), so we fix the source size to the value derived at 1 mm. This then results in a higher temperature ($248_{-18}^{+21} \text{ K}$) and higher column ($1.0 \pm 0.1 \times 10^{19} \text{ cm}^{-2}$) compared to both the 1 mm ($134 \pm 1 \text{ K}$ and $2.3 \pm 0.5 \times 10^{18} \text{ cm}^{-2}$) and the 2 mm data ($165 \pm 6 \text{ K}$ and $2.2 \pm 0.5 \times 10^{18} \text{ cm}^{-2}$) (see Figs. 5 and 6).

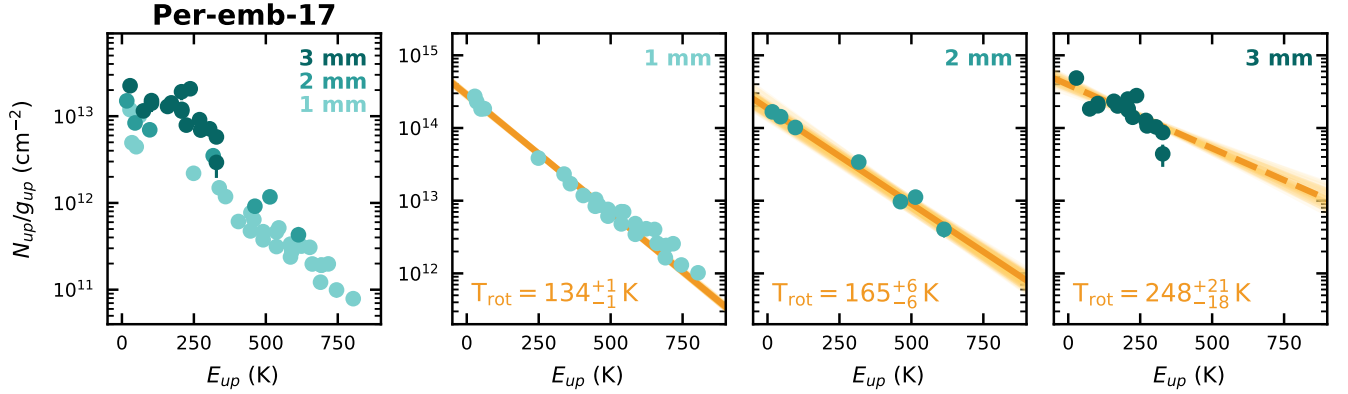


Figure 6. Rotation diagrams for CH_3OH at 1 mm (light teal), 2 mm (teal) and 3 mm (dark teal) toward Per-emb-17 (left panel) and results from a population diagram analysis of the observations at different wavelengths (three right most panels). The error bars correspond to 1σ , and are typically smaller than the symbols. Draws from the fit posteriors are shown with light orange lines, with the 50th percentiles shown as thick orange lines. The corresponding rotational temperature is listed in the bottom left corner. A solid line indicates that the rotational temperature, column density and source size were fitted, while a dashed line indicates that the source size was fixed (see Table 4 for details and all fit results). Rotation diagrams for all sources are presented in Fig. C5, and results from the population diagram analysis are shown in Figs. C6–C8.

Again, due to larger scatter (Ser-emb-8 and Ser-emb-11W) or few detections (Ser-emb-1 and Ser-emb-17) we cannot reliably fit the 3 mm data for the other sources. However, assuming a rotational temperature and source size equal to that obtained at 1 mm results in 3 mm columns a factor ~ 1.9 – 9.6 higher than at 1 mm (see also Fig. 5). For Ser-emb-17, the single detected transition cannot be reproduced with the rotational temperature and source size derived at 1 mm. No 3 mm transitions are detected toward HBC494 and Per-emb-20, but column density upper limits allow for columns a factor 1.0–5.4 higher at 3 mm (Table 4 and Fig. 5).

Taken together, the CH_3OH rotational temperature shows little variation among the sources in our sample (135–250 K) based on the transitions detected at 1 mm. For Per-emb-17, both the rotational temperature and the column density increase for transitions detected at longer wavelengths. The three other sources with multiple detections at 3 mm (Ser-emb-1, Ser-emb-8 and Ser-emb-11W) also show column density increases of a factor ~ 2 – 10 at 3 mm. This confirms the CH_3CN results that we are seeing hotter gas closer to the protostar at 3 mm.

4. DISCUSSION

For all eight sources in our sample with detections of CH_3CN and CH_3OH , the rotational temperature for CH_3CN is found to be higher than for CH_3OH (Fig. 4). In addition, the CH_3CN temperatures are generally higher, with rotational temperatures at 1 mm for CH_3CN ranging between ~ 280 – 425 K (except for Per-emb-17, where $T_{\text{rot}} = 195$ K, but with a strong indication of a second warmer component) and for CH_3OH between ~ 135 – 250 K. In Sect. 4.1, we will show that

this difference in rotational temperatures is indicative of different spatial distributions, with CH_3CN enhanced in hot gas. We will discuss potential origins of this enhancement in Sect. 4.2, arguing that it may be the result of carbon-grain sublimation. Finally, we will discuss in Sect. 4.3 that carbon-grain sublimation may then be common around low-mass protostars.

4.1. Spatial distribution of CH_3CN and CH_3OH

There is no correlation between rotational temperature and luminosity. While HOPS-370 is more than 50 times more luminous than the low-mass sources (except HBC494), the CH_3CN rotational temperature is only marginally higher and the CH_3OH rotational temperature is even amongst the lowest in the sample. This hints that CH_3CN emission is more effected by the source luminosity, and therefore potentially the presence of hot circumstellar material, than CH_3OH . Due to the weak emission toward HBC494, it is not possible to tell whether this source shows the same trend as HOPS-370 which has similar luminosity.

Since both molecules are observed simultaneously and transitions with a similar range of upper-level energies are covered, the observed difference in rotational temperature is not due to differences in instrumental setup. Instead, it points to a different spatial distribution of the molecules, with CH_3CN tracing hotter gas than CH_3OH . This could mean that CH_3CN has a more compact distribution than CH_3OH or that the CH_3CN abundance is enhanced in hot gas compared to cooler gas, while the CH_3OH abundance is more constant with radius or decreases at higher temperature. Difference in spatial extent or the radial intensity profile are not directly vis-

Table 4. Rotational temperatures, column densities and source sizes for CH₃OH.

Source	1 mm			2 mm			3 mm		
	T_{ex} (K)	N (cm ⁻²)	θ_s (arcsec)	T_{ex} (K)	N (cm ⁻²)	θ_s (arcsec)	T_{ex} (K)	N (cm ⁻²)	θ_s (arcsec)
HBC494	$\lesssim 223$	$\lesssim 1.1 \times 10^{17}$	[0.122] ^a	[223]	$< 6.1 \times 10^{17}$	[0.122] ^a
HOPS-370	160^{+3}_{-4}	$(6.6^{+1.0}_{-1.0}) \times 10^{18}$	$0.158^{+0.001}_{-0.001}$	131^{+15}_{-16}	$(1.3^{+0.4}_{-0.3}) \times 10^{19}$	$0.138^{+0.010}_{-0.007}$
Per-emb-17	134^{+1}_{-1}	$(2.3^{+0.5}_{-0.5}) \times 10^{18}$	$0.117^{+0.001}_{-0.001}$	165^{+6}_{-6}	$(2.2^{+0.5}_{-0.5}) \times 10^{18}$	$0.139^{+0.006}_{-0.005}$	248^{+21}_{-18}	$(1.0^{+0.1}_{-0.1}) \times 10^{19}$	[0.117]
Per-emb-20	154^{+7}_{-6}	$(1.8^{+0.4}_{-0.4}) \times 10^{18}$	$0.045^{+0.002}_{-0.002}$	[154]	$\sim 2.0 \times 10^{18}$	[0.045]	[154]	$< 1.7 \times 10^{18}$	[0.045]
Ser-emb-1	210^{+12}_{-11}	$(4.2^{+0.9}_{-0.9}) \times 10^{16}$	[0.225] ^a	[210]	$< 6.3 \times 10^{16}$	[0.225] ^a	[210]	$(3.3^{+0.7}_{-0.7}) \times 10^{17}$	[0.225] ^a
Ser-emb-8	169^{+7}_{-7}	$(5.1^{+1.2}_{-1.2}) \times 10^{18}$	$0.062^{+0.002}_{-0.002}$	[169]	$< 5.6 \times 10^{17}$	[0.062]	[169]	$(9.9^{+9.4}_{-3.9}) \times 10^{18}$	[0.062]
Ser-emb-11W	188^{+9}_{-9}	$(7.1^{+1.5}_{-1.5}) \times 10^{18}$	$0.063^{+0.002}_{-0.002}$	296^{+80}_{-32}	$(1.4^{+0.6}_{-0.4}) \times 10^{19}$	[0.063]	[296] ^b	$(6.8^{+1.5}_{-1.2}) \times 10^{19}$	[0.063]
Ser-emb-17	251^{+25}_{-19}	$(1.6^{+0.4}_{-0.4}) \times 10^{19}$	$0.038^{+0.002}_{-0.002}$	—	—	—	—	—	—

Notes. Rotational temperatures, column densities and source sizes obtained from population diagram analysis. Listed values and uncertainties correspond to the 50th, and 16th and 84th percentiles, respectively, of the posterior distributions. For the column densities, a flux calibration uncertainty (20% at 1 and 2 mm, 10% at 3 mm) has been added to the fit uncertainty through a root sum square. Values listed between square brackets are kept fixed at the value derived from the 1 mm transitions, unless noted otherwise. For sources with no detections at 2 and/or 3 mm, upper limits are calculated using the rotational temperature and source size derived from the 1 mm transitions. A dash (—) indicates that no column density could be determined. Three dots (...) indicate that a frequency range has not been observed. For HOPS-370, the combined fit to the 1 mm and 2 mm data combined results in 167 ± 2 K and $(7.2 \pm 0.1) \times 10^{18}$ cm⁻².

^a Source size fixed at deconvolved continuum size.

^b Temperature fixed at the value derived at 2 mm.

ible in our spatially unresolved observations, but we can assess the size of the emitting region using both optically thick and thin transitions, and the relative contributions from warm versus hot gas by comparing emission at 1 mm and 3 mm. The first strategy will be discussed in Sect. 4.1.1 and the second analysis in Sect. 4.1.2.

4.1.1. Emitting area

The emitting areas derived from the population diagram analysis are listed in Tables 3 and 4, and shown in Fig. 7. For CH₃CN, the emitting areas have radii between ~ 4 –13 au for the low-mass sources, although a larger radius of 32 au is found for Ser-emb-11W at 3 mm, and measures ~ 30 au for HOPS-370. The emitting area for CH₃OH is a few au larger for all sources. The emitting area generally increases for higher luminosities.

If the distribution of CH₃OH and CH₃CN is governed by thermal desorption, their emission should originate from within the water snowline since their binding energies are very similar to that of water (e.g., Collings et al. 2004; Wakelam et al. 2017; Das et al. 2018; Ferrero et al. 2020; Busch et al. 2022; Minissale et al. 2022). We can make an estimate of the snowline location based on the luminosity. Bisschop et al. (2007) has shown that the water snowline radius ($R = 100$ K) in high-mass protostars depend on luminosity via

$$R_{\text{snowline}} = 15.4 \sqrt{L_{\star}/L_{\odot}} \text{ au}, \quad (6)$$

and van 't Hoff et al. (2022) verified that the same relation holds for low-mass sources.

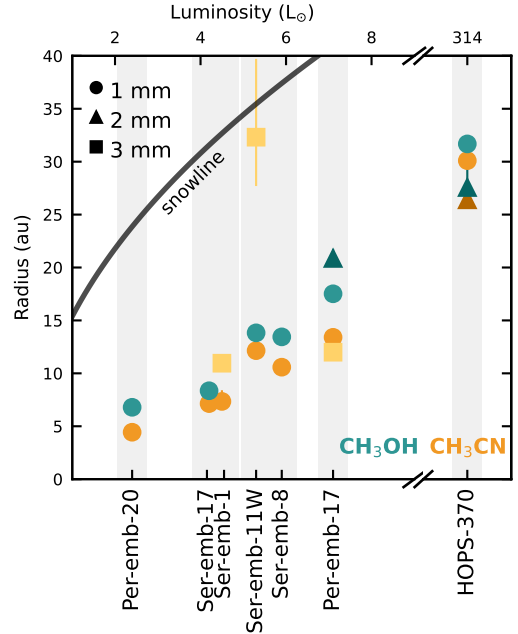


Figure 7. Overview of emitting areas derived from CH₃CN (orange) and CH₃OH (teal) as function of bolometric luminosity. Results from 1 mm observations ($J_K = 14_K - 13_K$ for CH₃CN) are shown as circles, results from 2 mm observations ($J_K = 12_K - 12_K$ for CH₃CN) as triangles, and results from 3 mm observations ($J_K = 5_K - 4_K$ for CH₃CN) as squares. The black line marks the expected water snowline location (100 K) in a protostellar envelope based on the bolometric luminosity (Eq. 6), as a proxy for the CH₃OH and CH₃CN snowlines. The vertical gray areas are meant to guide the eye.

It is clear from Fig. 7 that the expected water snowline location is more extended than the observed CH_3CN and CH_3OH emission. The snowline is expected at least 20 au further out for the lowest luminosity sources and more than 200 au further out for HOPS-370³. This could mean that the emission is more compact than expected from thermal desorption. Alternatively, the abundances in the inner region are enhanced over the abundances released from the ice, making the unresolved observations more sensitive to this inner region. The differences in emitting area and excitation temperature then suggest that the enhancement for CH_3CN is stronger and/or occurring at smaller radii than for CH_3OH .

However, if the continuum emission in the inner region is optically thick, the derived emitting area is likely not a spherical area centered on the source, but rather an annulus with an inner radius equal to the dust $\tau = 1$ radius (in the extreme case of no emission at all along our line of sight toward the source). The derived emitting area should then thus be considered an effective emitting area, and the radii shown in Fig. 7 are smaller than the actual spatial distributions. The much larger radius derived for Ser-emb-11W that is in good agreement with the expected snowline location may then indicate that the dust is optically thin at 3 mm toward this source.

Nevertheless, these results suggest that the distribution of CH_3CN is indeed different than that of CH_3OH as the dust optical depth is expected to equally affect both molecules, and a larger emitting area for CH_3OH due to more emission from smaller radii is inconsistent with the lower excitation temperatures. A similar conclusion is reached by Walls et al. (under review) for HOPS-370 using radiative transfer modeling with a physical structure appropriate for this source (Tobin et al. 2020). Observations with high enough angular resolution to at least resolve the snowline will be able to constrain whether the emission is indeed more extended that suggested by the derived emitting areas and potentially whether CH_3OH and CH_3CN have different spatial distributions.

4.1.2. Emission at different wavelengths

Another way to address differences in distribution between CH_3CN and CH_3OH is by comparing emission at

³ Equation 6 is likely not valid for HOPS-370 given the presence of a ~ 200 au gas-disk (Tobin et al. 2019), which changes the density and temperature structure compared to that of an envelope. In addition, the freeze-out temperature of water and COMs will be higher (~ 150 K) at the higher densities in the disk. Nonetheless, the temperature structure derived from detailed radiative transfer modeling by Tobin et al. (2020) still places the snowline outside of ~ 150 au.

different wavelengths (1 and 3 mm). Due to the lower dust opacity at longer wavelengths, emission close to the star can be visible at these wavelengths while being obscured by the dust at shorter wavelengths (see De Simone et al. 2020 for an comparison of NGC1333 IRAS4A at mm and cm wavelengths). For both CH_3CN and CH_3OH we derive higher column densities at 3 mm than at 1 mm (Fig. 5), and for Per-emb-17 we can derive rotational temperatures for CH_3OH at 1, 2 and 3 mm which increases with wavelength (Fig. 6). Overall, these results thus suggest that we indeed trace gas closer to the protostar at 3 mm.

However, while the increase in CH_3OH column is $\lesssim 10$, the CH_3CN column at 3 mm is more than ~ 10 times higher than at 1 mm toward at least four out of seven sources, with the largest enhancement a factor 46 for Ser-emb-1. This difference is not due to uncertainties in the flux calibration. A flux calibration uncertainty (20% at 1 and 2 mm, and 10% at 3 mm) has been included in the uncertainty on the column density, and the column density increase at 3 mm is at least a factor of two. Moreover, the CH_3CN and CH_3OH column densities at a given wavelength are obtained from the same observations. Nonetheless, to mitigate uncertainties in flux calibration altogether, we present the $\text{CH}_3\text{CN}/\text{CH}_3\text{OH}$ ratio for each source at both wavelengths in Fig. 8. This shows a clear increase in the $\text{CH}_3\text{CN}/\text{CH}_3\text{OH}$ ratio at 3 mm for Ser-emb-1 and Ser-emb-8, and a tentative increase for Per-emb-17 and Ser-emb-11W. In at least four out of the eight sources in our sample (as well as for HOPS-370; Walls et al., *subm.*) we thus see evidence that CH_3CN is enhanced in hot gas close to the protostar compared to CH_3OH .

4.2. Origin of CH_3CN enhancement in hot gas

From a chemical perspective, an enhancement of CH_3CN in hot gas relative to CH_3OH could be due to more effective destruction of CH_3CN in warm gas just inside the snowline, more effective destruction of CH_3OH in hot gas close to the star, or gas-phase formation of CH_3CN in hot gas. While the destruction by H_3^+ is approximately three times faster for CH_3CN than for CH_3OH (McElroy et al. 2013), the short timescales at these high densities ($< 10^5$ yr; Hatchell et al. 1998) would mean that a relative change in abundance would be visible only for a short period of time. Given that we observe a difference between CH_3CN and CH_3OH for both Class 0 and Class I protostars, more efficient gas-phase destruction of CH_3CN just inside the snowline is unlikely to be the origin.

Another destruction mechanism is photodissociation upon the desorption of UV photons, but since pho-

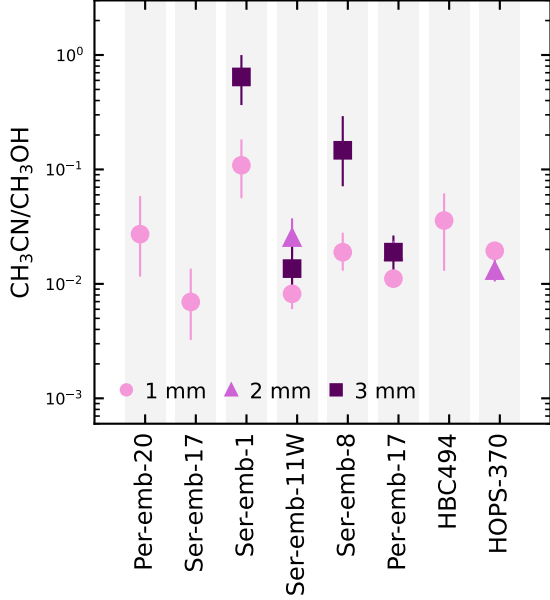


Figure 8. CH₃CN/CH₃OH column density ratio at 1 mm (pink circles), 2 mm (light purple triangles) and 3 mm (dark purple squares) toward the sources in our sample. The error bars take only the fit uncertainty into account since the CH₃CN and CH₃OH transitions are obtained from the same observations.

todissociation rates for CH₃CN and CH₃OH are similar (Heays et al. 2017, and references therein), this is not expected to result in an increased CH₃CN/CH₃OH ratio in hot gas. Because CH₃OH formation occurs solely in ices, unlike CH₃CN which can form in the gas, the CH₃OH abundance is expected to decrease once all ice has sublimated, especially when a disk is present and the radial migration of gas is slow (Aikawa et al. 2020). Although a detailed analysis of the radial abundance would be required for firm conclusions, the 2–10 times higher column densities at 3 mm (Fig. 5) do not immediately suggest a strong decrease of CH₃OH in the inner region. In addition, Tobin et al. (2020) and Walls et al. (subm.) show that the CH₃OH emission toward HOPS-370 can be reproduced with a constant abundance profile. More effective gas-phase destruction of CH₃OH is thus also unlikely to be the cause of the observed differences.

The relative enhancement of CH₃CN in hot gas is thus probably due to formation of CH₃CN at high temperatures. This is, for example, seen in the models by Garrod (2013); Garrod et al. (2017, 2022), where above ~300 K, H atoms can overcome the activation energy barrier to react efficiently with NH₃, NH₂ and NH, gradually increasing the amount of atomic nitrogen through abstraction of hydrogen. Atomic nitrogen then reacts with CH₃ to form HCN and subsequently CH₃CN. This

process depends on the presence of NH₃ (see also, e.g., Taquet et al. 2016), whose abundance in these models is substantially higher (17% with respect to H₂O ice) than observed toward low-mass protostars (3–10%; Boogert et al. 2015, and references therein) and dense clouds (~4–5%; McClure et al. 2023). In addition, a strong increase in CH₃CN is only visible in the slow warm-up models, where 300 K is reached after 10⁶ yr, which is longer than the protostellar lifetime of a few 10⁵ yr. For medium warm-up time scales, where 300 K is reached after 2 × 10⁵ yr, the increase in CH₃CN abundance is minimal even though there is a strong increase in HCN. It is therefore not clear whether these models can explain the observations presented here.

In the most recent models by Garrod et al. (2022) (labeled as “final” in that work), the HCN abundance is two orders of magnitude higher than the CH₃CN abundance in >300 K gas, and both molecules are expected to trace similar regions and conditions. We can therefore test some of these model predictions using the HC¹⁵N $J = 3 - 2$ transition at 258.156996 GHz covered in our 1 mm data sets (Fig. D2). Assuming optically thin emission in LTE and a conservative ¹⁴N/¹⁵N ratio of 440 as measured for the solar nebula (Marty et al. 2011)⁴, the HC¹⁵N $J = 3 - 2$ peak brightness temperature is expected to be 2.75 times higher than that for CH₃CN 14₄–13₄ at 300 K. In our observations, HC¹⁵N is fainter than CH₃CN 14₄–13₄ toward HOPS-370, of comparable brightness toward Per-emb-17 and Ser-emb-11W, and only brighter than CH₃CN 14₄–13₄ toward Per-emb-20, Ser-emb-1, Ser-emb-8 and Ser-emb-17. The strongest difference is observed toward Per-emb-20, but HC¹⁵N is only 1.7 times stronger than CH₃CN 14₄–13₄. The models by Garrod et al. appear thus not directly fully in agreement with our observations.

Another process that could be responsible for the enhancement of CH₃CN in the hot gas, potentially in tandem with the hot-gas chemistry in the Garrod et al. models, is the thermal destruction of carbonaceous grains and the subsequent release of carbon and nitrogen into the hot gas. The chemical models of protoplanetary disks by Wei et al. (2019) show that the additionally available carbon resulting from carbon-grain destruction strongly increases the HCN abundance. Although these authors do not discuss CH₃CN, their results suggest that an increase in HCN in hot gas is possible without having all nitrogen initially in NH₃. Alternatively, since

⁴ lower ¹⁴N/¹⁵N ratios of ~80–300 have been observed in the Solar System’s rocky planets, comets and meteorites (Mumma & Charnley 2011), as well as in protoplanetary disks (Guzmán et al. 2017; Hily-Blant et al. 2017)

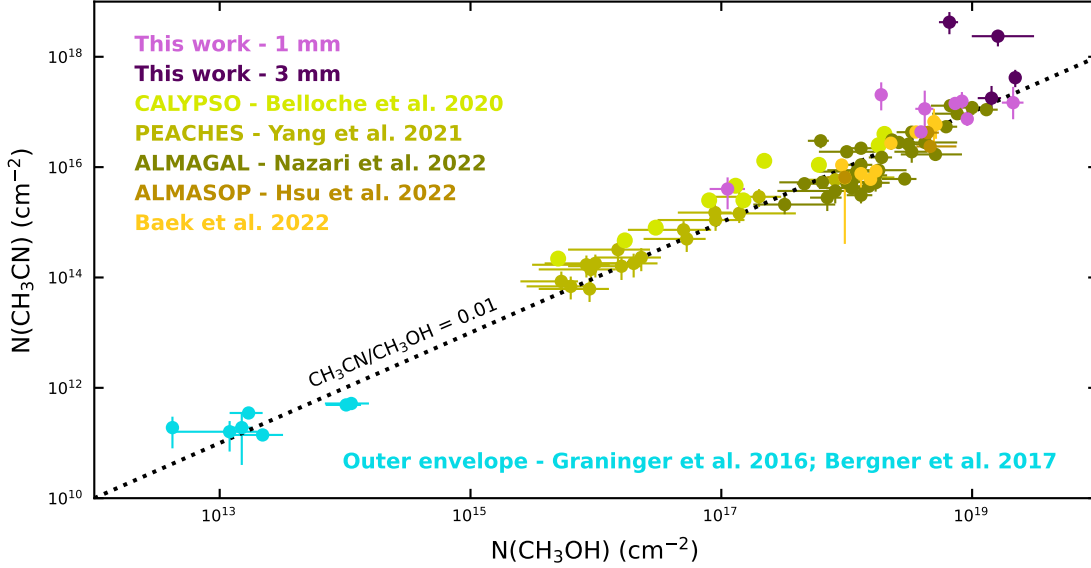


Figure 9. CH_3CN column densities versus CH_3OH column densities as derived in this work at 1 mm (purple) and 3 mm (dark purple) and from surveys of low and high-mass protostars in the recent literature (Graninger et al. 2016; Bergner et al. 2017; Belloche et al. 2020; Yang et al. 2021; Nazari et al. 2022; Hsu et al. 2022; Baek et al. 2022). For reference, the dotted line marks a $\text{CH}_3\text{CN}/\text{CH}_3\text{OH}$ column density ratio of 0.01.

it is unknown in what form carbon and nitrogen will be released upon grain destruction, the gas-phase NH_3 abundance in $\gtrsim 300$ K gas may be higher than the ice abundance due to carbon-grain sublimation. A detailed characterization of the chemistry in the warm and hot gas through both observations and models is required to constrain the origin of the CH_3CN enhancement.

4.3. The prevalence of carbon-grain sublimation

An enhancement of CH_3CN in hot gas was also found by Nazari et al. (2023) for high-mass protostars in the ALMAGAL survey. These authors determined the relative contribution of warm and hot gas by dividing the column density derived from transitions with low and high (> 400 K) upper-level energies. While the low-/high-energy column density ratio for CH_3OH was consistent with what would be expected from a uniform abundance within the snowline, the ratio was higher for CH_3CN . A similar result was found for the nitrogen-bearing species $\text{C}_2\text{H}_3\text{CN}$, while HNCO was similar to CH_3OH . A different distribution for CH_3CN and CH_3OH , with CH_3CN enhanced in hot gas, has now thus been found using two different analysis techniques and toward both low-mass (this work) and high-mass sources (Nazari et al. 2023), suggesting that this may be a common feature of protostellar chemistry.

Even though CH_3OH and CH_3CN are the most abundant oxygen- and nitrogen-bearing COM species, hot ($\gtrsim 300$ K) gas traced in particular by CH_3CN has not been widely reported toward low-mass protostars. This raises the question whether our sample is biased or whether

these signatures were not detectable with other studies. Since observations of COMs, even with ALMA, typically do not have the spatial resolution to resolve the emission, the focus has generally been on detection rates and a comparison of (relative) column densities amongst sources. For example, one of the first chemical surveys targeting a large number of low-mass protostars, CALYPSO, could only derive rotational temperatures for both CH_3OH and CH_3CN toward four out of the 12 sources with COM emission, because the 3 mm observations covering CH_3CN were typically not sensitive enough to detect $\nu_8 = 1$ transitions while the $\nu = 0$ transitions were often optically thick (Belloche et al. 2020). Ser-emb-8 was part of the CALYPSO sample, and the rotational temperature found for CH_3OH (210 ± 37 K) is consistent with the results presented here (231 ± 3 K). Our rotational temperature of 358 K for CH_3CN then suggests that hot gas may have gone undetected with the CALYPSO observations.

Moreover, high spectral resolution with ALMA typically comes at the cost of reduced bandwidth, which limits the number of transitions detected per source, such that excitation conditions cannot always be constrained. For example, the PEACHES survey of low-mass protostars in Perseus covered only three low-energy CH_3CN transitions ($14_K - 13_K$, with $K = 0 - 2$), preventing a temperature measurement (Yang et al. 2021). In addition, as the low K -transitions can get optically thick in colder gas, hot gas is thus also very likely to go undetected in the PEACHES survey.

Recent chemical surveys have found a tight correlation between column densities of CH_3OH and CH_3CN with $\text{CH}_3\text{CN}/\text{CH}_3\text{OH} \sim 0.01$ over seven orders of magnitude in column density and for both the outer envelope and the hot core (Fig. 9; Bergner et al. 2017; Belloche et al. 2020; Yang et al. 2021; Nazari et al. 2022; Hsu et al. 2022). At 1 mm, seven sources in our sample follow this trend very well, while one (Ser-emb-1) is located slightly above it (see also Fig. 8). Our targets are thus not standing out from those in previous samples. They are located at the higher end of the column density ranges because we constrained the emitting area. Interestingly, three sources that show an enhancement of CH_3CN in hot gas (Per-emb-17, Ser-emb-8 and Ser-emb-11W) follow the trend, while only one (Ser-emb-1) is slightly above it. The $\text{CH}_3\text{CN}/\text{CH}_3\text{OH}$ ratio at 1 mm alone is thus not informative about the presence of hot gas or a chemical signature of carbon-grain sublimation. This is reinforced by the three targets from the ALMASOP survey of Orion protostars, which all display rotational temperatures of 210–280 K for CH_3OH , while higher temperatures of 400–430 K are found for CH_3CN (measured from $^{13}\text{CH}_3\text{CN}$; Hsu et al. 2022). Hot gas and potential signatures of carbon-grain sublimation may thus have gone undetected in previous surveys and may be common based on the results presented here.

The ratios derived here at 3 mm (for Ser-emb-1 and Ser-emb-8) lie clearly above the trend, hinting that a $\text{CH}_3\text{CN}/\text{CH}_3\text{OH}$ ratio of ~ 0.01 may be reflective of the ice abundances, while the ratio increases in hot gas due to additional gas-phase formation of CH_3CN . However, detailed studies of larger source samples are required to confirm this as the $\text{CH}_3\text{CN}/\text{CH}_3\text{OH}$ ratio at 3 mm for Per-emb-17 and Ser-emb-11W are close to 0.01, and the CALYPSO observations analysed by Belloche et al. (2020) use 3 mm observations of CH_3CN as well (although CH_3OH observations at both 2 and 3 mm). The effects of, for example, the spatial extent and opacity of the continuum on the $\text{CH}_3\text{CN}/\text{CH}_3\text{OH}$ ratio would need to be studied in more detail, as the CALYPSO sources with COM detections have bright continuum emission which may shield the hot gas from our view even at 3 mm.

5. CONCLUSIONS

We have presented spatially unresolved NOEMA observations at 1, 2 and 3 mm of CH_3CN and CH_3OH toward nine low-mass protostars and one intermediate-mass protostar in different star-forming regions. Both molecules are detected toward seven of the low-mass protostars as well as toward the intermediate-mass protostar. The main findings from our analysis using population diagrams are as follows:

- Not all outbursting protostars display line-rich spectra, as only a few lines from both COMs and simple species are detected toward HBC494.
- Evidence of hot ($\gtrsim 300$ K) gas based on CH_3CN emission is found toward all eight sources, suggesting that hot gas may be common around (low-mass) protostars.
- Rotational temperatures are consistently higher for CH_3CN (~ 280 – 425 K) than for CH_3OH (~ 135 – 250 K), suggesting CH_3CN traces hotter gas than CH_3OH . There are no trends with source luminosity, but the intermediate-mass protostar displays the highest CH_3CN rotational temperature and an average CH_3OH rotational temperature, suggesting CH_3CN may be more strongly affected by the presence of hot gas than CH_3OH .
- The emitting area of CH_3CN is smaller than that for CH_3OH , hinting at a more compact distribution for CH_3CN or a CH_3CN enhancement close to the protostar.
- Higher column densities are traced at 3 mm compared to 1 mm for both CH_3CN and CH_3OH . In addition, in the only source with enough detections, the CH_3OH rotational temperature increased at longer wavelengths. These results suggest that hotter gas closer to the star is traced at longer wavelengths due to lower dust opacities. The increase in column density is stronger for CH_3CN than for CH_3OH , implying a stronger increase of CH_3CN in hot gas.

All together, these results suggests that hot $\gtrsim 300$ K gas is common around low and intermediate-mass protostars and that optically thin high- K transitions of CH_3CN , preferentially at longer wavelengths, are required to trace this gas. If carbon-grain sublimation would be the cause of the enhancement of CH_3CN in this hot gas then the early formation conditions of Earth may not be rare.

ACKNOWLEDGMENTS

The authors thank the referee for suggestions that improved the manuscript. M.L.R.H. would like to thank Ryan Loomis and Brett McGuire for discussing the analysis of CH_3CN emission and acknowledges support from the Michigan Society of Fellows.

REFERENCES

- Aikawa, Y., Furuya, K., Yamamoto, S., & Sakai, N. 2020, *ApJ*, 897, 110, doi: [10.3847/1538-4357/ab994a](https://doi.org/10.3847/1538-4357/ab994a)
- Anderson, D. E., Bergin, E. A., Blake, G. A., et al. 2017, *ApJ*, 845, 13, doi: [10.3847/1538-4357/aa7da1](https://doi.org/10.3847/1538-4357/aa7da1)
- Baek, G., Lee, J.-E., Hirota, T., Kim, K.-T., & Kim, M. K. 2022, *ApJ*, 939, 84, doi: [10.3847/1538-4357/ac81d3](https://doi.org/10.3847/1538-4357/ac81d3)
- Belloche, A., Maury, A. J., Maret, S., et al. 2020, arXiv e-prints, arXiv:2002.00592. <https://arxiv.org/abs/2002.00592>
- Bergin, E. A., Blake, G. A., Ciesla, F., Hirschmann, M. M., & Li, J. 2015, *Proceedings of the National Academy of Science*, 112, 8965, doi: [10.1073/pnas.1500954112](https://doi.org/10.1073/pnas.1500954112)
- Bergner, J. B., Martín-Doménech, R., Öberg, K. I., et al. 2019, *ACS Earth and Space Chemistry*, 3, 1564, doi: [10.1021/acsearthspacechem.9b00059](https://doi.org/10.1021/acsearthspacechem.9b00059)
- Bergner, J. B., Öberg, K. I., Garrod, R. T., & Graninger, D. M. 2017, *ApJ*, 841, 120, doi: [10.3847/1538-4357/aa72f6](https://doi.org/10.3847/1538-4357/aa72f6)
- Binkert, F., & Birnstiel, T. 2023, *MNRAS*, 520, 2055, doi: [10.1093/mnras/stad182](https://doi.org/10.1093/mnras/stad182)
- Bisschop, S. E., Jørgensen, J. K., van Dishoeck, E. F., & de Wachter, E. B. M. 2007, *A&A*, 465, 913, doi: [10.1051/0004-6361:20065963](https://doi.org/10.1051/0004-6361:20065963)
- Boogert, A. C. A., Gerakines, P. A., & Whittet, D. C. B. 2015, *ARA&A*, 53, 541, doi: [10.1146/annurev-astro-082214-122348](https://doi.org/10.1146/annurev-astro-082214-122348)
- Bouvier, M., Ceccarelli, C., López-Sepulcre, A., et al. 2022, *ApJ*, 929, 10, doi: [10.3847/1538-4357/ac5904](https://doi.org/10.3847/1538-4357/ac5904)
- Busch, L. A., Belloche, A., Garrod, R. T., Müller, H. S. P., & Menten, K. M. 2022, *A&A*, 665, A96, doi: [10.1051/0004-6361/202243383](https://doi.org/10.1051/0004-6361/202243383)
- Cazzoli, G., & Puzzarini, C. 2006, *Journal of Molecular Spectroscopy*, 240, 153, doi: [10.1016/j.jms.2006.09.013](https://doi.org/10.1016/j.jms.2006.09.013)
- Chini, R., Reipurth, B., Ward-Thompson, D., et al. 1997, *ApJL*, 474, L135, doi: [10.1086/310436](https://doi.org/10.1086/310436)
- Collings, M. P., Anderson, M. A., Chen, R., et al. 2004, *MNRAS*, 354, 1133, doi: [10.1111/j.1365-2966.2004.08272.x](https://doi.org/10.1111/j.1365-2966.2004.08272.x)
- Das, A., Sil, M., Gorai, P., Chakrabarti, S. K., & Loison, J. C. 2018, *ApJS*, 237, 9, doi: [10.3847/1538-4365/aac886](https://doi.org/10.3847/1538-4365/aac886)
- De Simone, M., Ceccarelli, C., Codella, C., et al. 2020, *ApJL*, 896, L3, doi: [10.3847/2041-8213/ab8d41](https://doi.org/10.3847/2041-8213/ab8d41)
- Enoch, M. L., Evans, Neal J. I., Sargent, A. I., & Glenn, J. 2009, *ApJ*, 692, 973, doi: [10.1088/0004-637X/692/2/973](https://doi.org/10.1088/0004-637X/692/2/973)
- Ferrero, S., Zamirri, L., Ceccarelli, C., et al. 2020, *ApJ*, 904, 11, doi: [10.3847/1538-4357/abb953](https://doi.org/10.3847/1538-4357/abb953)
- Foreman-Mackey, D., Hogg, D. W., Lang, D., & Goodman, J. 2013, *PASP*, 125, 306, doi: [10.1086/670067](https://doi.org/10.1086/670067)
- Fraser, H. J., Collings, M. P., McCoustra, M. R. S., & Williams, D. A. 2001, *MNRAS*, 327, 1165, doi: [10.1046/j.1365-8711.2001.04835.x](https://doi.org/10.1046/j.1365-8711.2001.04835.x)
- Furlan, E., Fischer, W. J., Ali, B., et al. 2016, *ApJS*, 224, 5, doi: [10.3847/0067-0049/224/1/5](https://doi.org/10.3847/0067-0049/224/1/5)
- Gail, H.-P., & Tieloff, M. 2017, *A&A*, 606, A16, doi: [10.1051/0004-6361/201730480](https://doi.org/10.1051/0004-6361/201730480)
- Garrod, R. T. 2013, *ApJ*, 765, 60, doi: [10.1088/0004-637X/765/1/60](https://doi.org/10.1088/0004-637X/765/1/60)
- Garrod, R. T., Belloche, A., Müller, H. S. P., & Menten, K. M. 2017, *A&A*, 601, A48, doi: [10.1051/0004-6361/201630254](https://doi.org/10.1051/0004-6361/201630254)
- Garrod, R. T., Jin, M., Matis, K. A., et al. 2022, *ApJS*, 259, 1, doi: [10.3847/1538-4365/ac3131](https://doi.org/10.3847/1538-4365/ac3131)
- Geiss, J. 1987, *A&A*, 187, 859
- Goldsmith, P. F., & Langer, W. D. 1999, *ApJ*, 517, 209, doi: [10.1086/307195](https://doi.org/10.1086/307195)
- Graninger, D. M., Wilkins, O. H., & Öberg, K. I. 2016, *ApJ*, 819, 140, doi: [10.3847/0004-637X/819/2/140](https://doi.org/10.3847/0004-637X/819/2/140)
- Guzmán, V. V., Öberg, K. I., Huang, J., Loomis, R., & Qi, C. 2017, *ApJ*, 836, 30, doi: [10.3847/1538-4357/836/1/30](https://doi.org/10.3847/1538-4357/836/1/30)
- Hatchell, J., Thompson, M. A., Millar, T. J., & MacDonald, G. H. 1998, *A&AS*, 133, 29, doi: [10.1051/aas:1998309](https://doi.org/10.1051/aas:1998309)
- Heays, A. N., Bosman, A. D., & van Dishoeck, E. F. 2017, *A&A*, 602, A105, doi: [10.1051/0004-6361/201628742](https://doi.org/10.1051/0004-6361/201628742)
- Hily-Blant, P., Magalhaes, V., Kastner, J., et al. 2017, *A&A*, 603, L6, doi: [10.1051/0004-6361/201730524](https://doi.org/10.1051/0004-6361/201730524)
- Hirschmann, M. M. 2016, *American Mineralogist*, 101, 540, doi: [10.2138/am-2016-5452](https://doi.org/10.2138/am-2016-5452)
- Hirschmann, M. M., & Dasgupta, R. 2009, *Chemical Geology*, 262, 4, doi: [10.1016/j.chemgeo.2009.02.008](https://doi.org/10.1016/j.chemgeo.2009.02.008)
- Hsieh, T.-H., Murillo, N. M., Belloche, A., et al. 2019, *ApJ*, 884, 149, doi: [10.3847/1538-4357/ab425a](https://doi.org/10.3847/1538-4357/ab425a)
- Hsu, S.-Y., Liu, S.-Y., Liu, T., et al. 2022, *ApJ*, 927, 218, doi: [10.3847/1538-4357/ac49e0](https://doi.org/10.3847/1538-4357/ac49e0)
- Jørgensen, J. K., van der Wiel, M. H. D., Coutens, A., et al. 2016, *A&A*, 595, A117, doi: [10.1051/0004-6361/201628648](https://doi.org/10.1051/0004-6361/201628648)
- Klarmann, L., Ormel, C. W., & Dominik, C. 2018, *A&A*, 618, L1, doi: [10.1051/0004-6361/201833719](https://doi.org/10.1051/0004-6361/201833719)
- Kress, M. E., Tielens, A. G. G. M., & Frenklach, M. 2010, *Advances in Space Research*, 46, 44, doi: [10.1016/j.asr.2010.02.004](https://doi.org/10.1016/j.asr.2010.02.004)
- Lee, J.-E., Lee, S., Baek, G., et al. 2019, *Nature Astronomy*, 3, 314, doi: [10.1038/s41550-018-0680-0](https://doi.org/10.1038/s41550-018-0680-0)
- Li, J., Bergin, E. A., Blake, G. A., Ciesla, F. J., & Hirschmann, M. M. 2021, *Science Advances*, 7, eabd3632, doi: [10.1126/sciadv.abd3632](https://doi.org/10.1126/sciadv.abd3632)

- Loomis, R. A., Cleeves, L. I., Öberg, K. I., et al. 2018, *ApJ*, 859, 131, doi: [10.3847/1538-4357/aac169](https://doi.org/10.3847/1538-4357/aac169)
- Martín-Doménech, R., Bergner, J. B., Öberg, K. I., et al. 2021, *ApJ*, 923, 155, doi: [10.3847/1538-4357/ac26b9](https://doi.org/10.3847/1538-4357/ac26b9)
- Marty, B., Chaussidon, M., Wiens, R. C., Jurewicz, A. J. G., & Burnett, D. S. 2011, *Science*, 332, 1533, doi: [10.1126/science.1204656](https://doi.org/10.1126/science.1204656)
- McClure, M. K., Rocha, W. R. M., Pontoppidan, K. M., et al. 2023, *Nature Astronomy*, 7, 431, doi: [10.1038/s41550-022-01875-w](https://doi.org/10.1038/s41550-022-01875-w)
- McElroy, D., Walsh, C., Markwick, A. J., et al. 2013, *A&A*, 550, A36, doi: [10.1051/0004-6361/201220465](https://doi.org/10.1051/0004-6361/201220465)
- Megías, A., Jiménez-Serra, I., Martín-Pintado, J., et al. 2023, *MNRAS*, 519, 1601, doi: [10.1093/mnras/stac3449](https://doi.org/10.1093/mnras/stac3449)
- Milam, S. N., Savage, C., Brewster, M. A., Ziurys, L. M., & Wyckoff, S. 2005, *ApJ*, 634, 1126, doi: [10.1086/497123](https://doi.org/10.1086/497123)
- Minh, Y. C., Irvine, W. M., Ohishi, M., et al. 1993, *A&A*, 267, 229
- Minissale, M., Aikawa, Y., Bergin, E., et al. 2022, *ACS Earth and Space Chemistry*, 6, 597, doi: [10.1021/acsearthspacechem.1c00357](https://doi.org/10.1021/acsearthspacechem.1c00357)
- Müller, H. S. P., Drouin, B. J., & Pearson, J. C. 2009, *A&A*, 506, 1487, doi: [10.1051/0004-6361/200912932](https://doi.org/10.1051/0004-6361/200912932)
- Müller, H. S. P., Brown, L. R., Drouin, B. J., et al. 2015, *Journal of Molecular Spectroscopy*, 312, 22, doi: [10.1016/j.jms.2015.02.009](https://doi.org/10.1016/j.jms.2015.02.009)
- Mumma, M. J., & Charnley, S. B. 2011, *ARA&A*, 49, 471, doi: [10.1146/annurev-astro-081309-130811](https://doi.org/10.1146/annurev-astro-081309-130811)
- Nakano, H., Kouchi, A., Tachibana, S., & Tsuchiyama, A. 2003, *ApJ*, 592, 1252, doi: [10.1086/375856](https://doi.org/10.1086/375856)
- Nazari, P., Tabone, B., van't Hoff, M. L. R., Jørgensen, J. K., & van Dishoeck, E. F. 2023, *ApJL*, 951, L38, doi: [10.3847/2041-8213/acdde4](https://doi.org/10.3847/2041-8213/acdde4)
- Nazari, P., Meijerhof, J. D., van Gelder, M. L., et al. 2022, *A&A*, 668, A109, doi: [10.1051/0004-6361/202243788](https://doi.org/10.1051/0004-6361/202243788)
- Ortiz-León, G. N., Loinard, L., Dzib, S. A., et al. 2018a, *ApJ*, 865, 73, doi: [10.3847/1538-4357/aada49](https://doi.org/10.3847/1538-4357/aada49)
- . 2018b, *ApJL*, 869, L33, doi: [10.3847/2041-8213/aaf6ad](https://doi.org/10.3847/2041-8213/aaf6ad)
- Penteado, E. M., Walsh, C., & Cuppen, H. M. 2017, *ApJ*, 844, 71, doi: [10.3847/1538-4357/aa78f9](https://doi.org/10.3847/1538-4357/aa78f9)
- Pollack, J. B., Hollenbach, D., Beckwith, S., et al. 1994, *ApJ*, 421, 615, doi: [10.1086/173677](https://doi.org/10.1086/173677)
- Reipurth, B., & Bally, J. 1986, *Nature*, 320, 336, doi: [10.1038/320336a0](https://doi.org/10.1038/320336a0)
- Reipurth, B., Rodríguez, L. F., & Chini, R. 1999, *AJ*, 118, 983, doi: [10.1086/300958](https://doi.org/10.1086/300958)
- Rubin, M., Altwegg, K., Balsiger, H., et al. 2019, *MNRAS*, 489, 594, doi: [10.1093/mnras/stz2086](https://doi.org/10.1093/mnras/stz2086)
- Segura-Cox, D. M., Schmiedeke, A., Pineda, J. E., et al. 2020, *Nature*, 586, 228, doi: [10.1038/s41586-020-2779-6](https://doi.org/10.1038/s41586-020-2779-6)
- Shirley, Y. L. 2015, *PASP*, 127, 299, doi: [10.1086/680342](https://doi.org/10.1086/680342)
- Strom, K. M., & Strom, S. E. 1993, *ApJL*, 412, L63, doi: [10.1086/186941](https://doi.org/10.1086/186941)
- Tabone, B., Bettoni, G., van Dishoeck, E. F., et al. 2023, *Nature Astronomy*, doi: [10.1038/s41550-023-01965-3](https://doi.org/10.1038/s41550-023-01965-3)
- Taquet, V., López-Sepulcre, A., Ceccarelli, C., et al. 2015, *ApJ*, 804, 81, doi: [10.1088/0004-637X/804/2/81](https://doi.org/10.1088/0004-637X/804/2/81)
- Taquet, V., Wirstrom, E. S., & Charnley, S. B. 2016, *ApJ*, 821, 46, doi: [10.3847/0004-637X/821/1/46](https://doi.org/10.3847/0004-637X/821/1/46)
- Tobin, J. J., Looney, L. W., Li, Z.-Y., et al. 2016, *ApJ*, 818, 73, doi: [10.3847/0004-637X/818/1/73](https://doi.org/10.3847/0004-637X/818/1/73)
- Tobin, J. J., Megeath, S. T., van't Hoff, M., et al. 2019, *ApJ*, 886, 6, doi: [10.3847/1538-4357/ab498f](https://doi.org/10.3847/1538-4357/ab498f)
- Tobin, J. J., Sheehan, P. D., Reynolds, N., et al. 2020, *ApJ*, 905, 162, doi: [10.3847/1538-4357/abc5bf](https://doi.org/10.3847/1538-4357/abc5bf)
- Tychoniec, L., Manara, C. F., Rosotti, G. P., et al. 2020, *A&A*, 640, A19, doi: [10.1051/0004-6361/202037851](https://doi.org/10.1051/0004-6361/202037851)
- van 't Hoff, M. L. R., Bergin, E. A., Jørgensen, J. K., & Blake, G. A. 2020, *ApJL*, 897, L38, doi: [10.3847/2041-8213/ab9f97](https://doi.org/10.3847/2041-8213/ab9f97)
- van 't Hoff, M. L. R., Tobin, J. J., Trapman, L., et al. 2018, *ApJL*, 864, L23, doi: [10.3847/2041-8213/aadb8a](https://doi.org/10.3847/2041-8213/aadb8a)
- van 't Hoff, M. L. R., Harsono, D., van Gelder, M. L., et al. 2022, *ApJ*, 924, 5, doi: [10.3847/1538-4357/ac3080](https://doi.org/10.3847/1538-4357/ac3080)
- Vastel, C., Loison, J. C., Wakelam, V., & Lefloch, B. 2019, *A&A*, 625, A91, doi: [10.1051/0004-6361/201935010](https://doi.org/10.1051/0004-6361/201935010)
- Wakelam, V., Loison, J. C., Mereau, R., & Ruaud, M. 2017, *Molecular Astrophysics*, 6, 22, doi: [10.1016/j.molap.2017.01.002](https://doi.org/10.1016/j.molap.2017.01.002)
- Wasson, J. T., & Kallemeyn, G. W. 1988, *Philosophical Transactions of the Royal Society of London Series A*, 325, 535, doi: [10.1098/rsta.1988.0066](https://doi.org/10.1098/rsta.1988.0066)
- Wei, C.-E., Nomura, H., Lee, J.-E., et al. 2019, *ApJ*, 870, 129, doi: [10.3847/1538-4357/aaf390](https://doi.org/10.3847/1538-4357/aaf390)
- Xu, L.-H., Fisher, J., Lees, R. M., et al. 2008, *Journal of Molecular Spectroscopy*, 251, 305, doi: [10.1016/j.jms.2008.03.017](https://doi.org/10.1016/j.jms.2008.03.017)
- Yang, Y.-L., Sakai, N., Zhang, Y., et al. 2021, *ApJ*, 910, 20, doi: [10.3847/1538-4357/abdfd6](https://doi.org/10.3847/1538-4357/abdfd6)

Table A1. NOEMA observing log.

NOEMA program	Sources	Date	Config.	Bandpass calibrator	Phase calibrator	Flux calibrator	Spectral setting ^a	Time on source (hour)
W19AA	HBC494	14 Feb 2020	10A	3C84	J0542-0913	LKHA101	1 mm	2.2
	HCB494	22 Feb 2020	10A	3C84	J0542-0913	LKHA101	1 mm	1.1
	Per-emb-17, Per-emb-20	05 Feb 2020	10A	3C84	0333+321	LKHA101	1 mm	0.6, 1.2
	Per-emb-17, Per-emb-20	06 Feb 2020	10A	3C454.3	0333+321	MWC349	1 mm	2.2, 4.5
	Ser-emb-1, Ser-emb-8, Ser-emb-17	07 Feb 2020	10A	3C345	1827+062	MWC349	1 mm	1.0, 1.0, 1.0
	Ser-emb-1, Ser-emb-8, Ser-emb-17	15 Feb 2020	10A	3C273	1827+062	MWC349	1 mm	1.0, 1.0, 1.0
	Ser-emb-1, Ser-emb-8, Ser-emb-17	18 Feb 2020	10A	1749+096	1827+062	MWC349	1 mm	0.8, 0.8, 0.8
	Ser-emb-1, Ser-emb-8, Ser-emb-17	20 Feb 2020	10A	3C84	1827+062	MWC349	1 mm	1.2, 1.2, 1.2
W20AD	HBC494	15 Feb 2021	11A	3C84	J0542-0913	LKHA101	3 mm	3.4
	Per-emb-17, Per-emb-20	16 Feb 2021	10A	3C84	0333+321, 0322+222	MWC349	3 mm	2.1, 2.1
	Ser-emb-1, Ser-emb-8, Ser-emb-17	09 Feb 2021	11A	3C345	1801+010, 1851+0035	MWC349	3 mm	0.7, 0.6, 0.5
	Ser-emb-1, Ser-emb-8, Ser-emb-17	17 Feb 2021	11A	3C345	1801+010, 1851+0035	MWC349	3 mm	1.0, 1.0, 1.0
	Ser-emb-1, Ser-emb-8, Ser-emb-17	23 Feb 2021	11A	3C345	1801+010, 1851+0035	3C345	3 mm	1.2, 1.2, 1.2
W20AE	Per-emb-17, Per-emb-20	03 Mar 2021	11A	3C84	0333+321, 0322+222	MWC349	2 mm	0.8, 0.8
W20AF	HOPS-370	23 Dec 2020	11C	3C84	J0542-0913, 0458-020	LKHA101	1 mm	3.0
	HOPS-370	06 Jan 2021	11C	3C84	J0542-0913, 0458-020	MWC349	1 mm	1.9
	HOPS-370	17 Feb 2021	10A	3C84	J0542-0913, 0458-020	LKHA101	1 mm	2.6
	HOPS-370	18 Mar 2021	11A	3C84	J0542-0913, 0458-020	LKHA101	2 mm	2.2
S21AH	Ser-emb-1, Ser-emb-8, Ser-emb-17	19 Nov 2021	9C	2013+370	1801+010, 1851+0035	MWC349	2 mm	0.9, 0.9, 1.0
	Ser-emb-1, Ser-emb-8, Ser-emb-17	20 Nov 2021	9C	3C273	1801+010, 1851+0035	MWC349	2 mm	1.1, 1.1, 1.1

Notes. Ser-emb-11W is observed in the same field of view as Ser-emb-17.

^a Each spectral setup consists of two ~ 8 GHz wide sidebands with 2 MHz spectral resolution, and a set of narrow high spectral resolution windows (62.5 kHz resolution). The 1 mm setting covers the frequency ranges of 240.9–248.6 GHz and 256.4–264.1 GHz, the 2 mm setting covers the frequency ranges of 202.7–210.8 GHz and 218.2–226.3 GHz, and the 3 mm setting covers the frequency ranges of 85.2–93.3 GHz and 100.7–108.8 GHz. Here we focus on the 2 MHz resolution data, except for CH₃CN $J = 5 - 4$, where we use a high spectral resolution window between 91.92–92.01 GHz, binned to 2 km s⁻¹.

APPENDIX

A. NOEMA OBSERVING LOG

Details of the NOEMA observations are presented in Table A1.

B. LINE FITTING

Individual line fluxes are measured by fitting a Gaussian to the line profile using the CLASS package of GILDAS. For CH₃CN, the relative positions of the different K -components for each J -transition are kept fixed, and one line width is enforced for all K -components. The line width fit for the different J -transitions is generally consistent per source, especially between $14_K - 13_K$ and $12_K - 11_K$. The broadest lines are observed toward HOPS-370 and Per-emb-17 (~ 11 km s⁻¹), and the Serpens sources display the most narrow lines (~ 5 – 6 km s⁻¹). The linewidth toward HBC494 and Per-emb-20 is ~ 9 km s⁻¹. The linewidths are typically slightly smaller at 3 mm, probably due to the lower signal-to-noise of these observations. The obtained linewidths and integrated fluxes are listed in Tables B1 and B2, respectively.

The CH₃OH transitions are more spread out in frequency space than individual CH₃CN J -ladders. Hence,

Table B1. Line widths of the CH₃CN emission.

Source	1 mm ($J = 14 - 13$)	2mm ($J = 12 - 11$)	3 mm ($J = 5 - 4$)
HBC494	9.3 ± 0.9	...	–
HOPS-370	11.5 ± 0.1	11.9 ± 0.1	...
Per-emb-17	11.1 ± 0.1	10.6 ± 0.2	8.4 ± 0.4
Per-emb-20	9.4 ± 0.3	–	–
Ser-emb-1	5.0 ± 0.2	4.4 ± 0.4	6.8 ± 0.5
Ser-emb-8	6.4 ± 0.2	7.2 ± 0.8	3.6 ± 0.3
Ser-emb-11W	5.4 ± 0.1	5.4 ± 0.3	4.0 ± 0.1
Ser-emb-17	6.2 ± 0.3	–	–

Notes. Line widths in km s⁻¹ obtained from Gaussian fits. Three dots (...) indicate that a frequency range has not been observed, and a dash (–) indicates that no transitions are detected.

we keep the line center as free parameter when fitting Gaussians to obtain the integrated flux, but fix the line width to the width derived for CH₃CN in the same

dataset. This aids the fit of weak lines and lines in crowded regions of the spectrum, but does not change the overall results compared to when the linewidth is kept as free parameter. Blended transitions are excluded from the analysis. While we use the high spectral resolution 3 mm spectra for CH₃CN $5_K - 4_K$, the majority of CH₃OH lines in the 3 mm dataset are not covered at high spectral resolution so we use the low-resolution (2 MHz) dataset. For Ser-emb-8 and Ser-emb-11W, the narrow lines are then detected only in 1–2 channels at 3 mm. Instead of a Gaussian fit, we estimate their line flux by multiplying the peak intensity by the CH₃CN line width. Integrated fluxes for the observed CH₃OH transitions that are not blended and used in the analysis are listed in Table B3.

Molecular line parameters and the partition function for CH₃CN are obtained from the Cologne Database

for Molecular Spectroscopy (CDMS; Müller et al. 2015), which uses data from Cazzoli & Puzzarini (2006) and Müller et al. (2009). The 2016 version of the CDMS line list for CH₃CN treats the double statistical weight of the $K = 3, 6, 9, \dots$ transitions by listing two entries for these transitions, both with g_{up} equal to g_{up} of the other K -transitions. To properly account for optical depth, we treat the $K = 3, 6, 9, \dots$ transitions as one transition with double the statistical weight of the other K -transitions. This means we replace the two entries for the $K = 3, 6, 9, \dots$ transitions by one that has the combined intensity and g_{up} of the two individual entries. The molecular line parameters are listed in Table B2. Molecular line parameters for CH₃OH are also obtained from CDMS, which are based on data from Xu et al. (2008). The partition function includes both symmetry states as well as the $\nu_t = 0 - 2$ torsional states (see Table B3).

Table B2. Spectroscopic parameters and integrated intensities for the observed CH₃CN transitions.

Transition	Frequency (GHz)	E_{up} (K)	g_{up}	A_{ul} ($\log_{10}(\text{s}^{-1})$)	HBC494	HOPS-370	Per-emb-17	Per-emb-20	W (K km s ⁻¹)			
									Ser-emb-1	Ser-emb-8	Ser-emb-11W	Ser-emb-17
50 – 40	91.987088	13	22	-4.20	–	...	10.7 ± 1.2	–	3.8 ± 0.5	1.7 ± 0.4	5.1 ± 0.5	–
51 – 41	91.985314	20	22	-4.22	–	...	5.6 ± 1.1	–	2.1 ± 0.5	–	6.2 ± 0.5	–
52 – 42	91.979995	42	22	-4.27	–	...	6.0 ± 1.0	–	4.0 ± 0.6	2.6 ± 0.5	6.4 ± 0.5	–
53 – 43	91.971131	78	44	-4.39	–	...	7.3 ± 1.1	–	3.1 ± 0.5	2.1 ± 0.5	7.1 ± 0.5	–
54 – 44	91.958726	128	22	-4.64	–	...	3.4 ± 1.0	–	2.2 ± 0.5	–	1.9 ± 0.5	–
120 – 110	220.747262	69	50	-3.03	–	17.6 ± 0.8	27.0 ± 2.0	–	2.3 ± 0.7	3.1 ± 1.0	4.7 ± 0.9	–
121 – 111	220.743011	76	50	-3.04	–	24.3 ± 0.9	25.7 ± 2.1	–	5.4 ± 0.8	4.3 ± 1.2	5.3 ± 1.0	–
122 – 112	220.730261	97	50	-3.05	–	22.9 ± 0.6	28.3 ± 1.6	–	2.7 ± 0.8	5.6 ± 1.0	4.8 ± 1.0	–
123 – 113	220.709017	133	100	-3.06	–	25.5 ± 0.6	27.4 ± 1.6	–	4.4 ± 0.8	3.5 ± 1.0	5.9 ± 0.9	–
124 – 114	220.679287	183	50	-3.09	–	17.7 ± 0.6	22.9 ± 1.6	–	–	4.7 ± 1.0	4.0 ± 0.9	–
125 – 115	220.641084	247	50	-3.12	–	18.6 ± 1.5	15.8 ± 1.6	–	–	3.7 ± 1.0	3.1 ± 0.9	–
126 – 116	220.594424	326	100	-3.16	–	18.0 ± 1.9	blended	–	1.8 ± 0.7	–	3.5 ± 0.9	–
127 – 117	220.539324	419	50	-3.22	–	7.7 ± 0.2	4.1 ± 1.4	–	–	–	2.3 ± 0.8	–
128 – 118	220.475808	526	50	-3.29	–	5.2 ± 0.5	–	–	–	–	–	–
129 – 119	220.403901	647	100	-3.39	–	blended	–	–	–	–	–	–
1210 – 1110	220.323631	782	50	-3.55	–	2.3 ± 0.4	–	–	–	–	–	–
140 – 130	257.527384	93	58	-2.83	3.6 ± 1.8	23.0 ± 0.3	65.3 ± 2.8	8.3 ± 1.2	10.9 ± 0.8	18.1 ± 1.4	14.1 ± 0.8	12.6 ± 1.1
141 – 131	257.522428	100	58	-2.83	4.7 ± 1.9	30.2 ± 0.2	82.9 ± 2.6	11.3 ± 1.2	12.3 ± 0.9	22.7 ± 1.4	17.6 ± 0.9	8.2 ± 1.1
142 – 132	257.507562	121	58	-2.84	3.5 ± 1.5	28.8 ± 0.3	72.5 ± 2.1	10.0 ± 1.0	8.1 ± 0.8	18.4 ± 1.4	16.8 ± 0.9	11.0 ± 1.1
143 – 133	257.482792	157	116	-2.85	5.9 ± 1.7	31.9 ± 0.3	82.4 ± 2.2	12.2 ± 1.0	9.3 ± 0.9	21.5 ± 1.4	16.6 ± 0.8	10.0 ± 1.1
144 – 134	257.448128	207	58	-2.87	2.5 ± 1.4	21.2 ± 0.3	48.8 ± 2.1	5.8 ± 1.0	6.2 ± 0.8	15.3 ± 1.3	9.4 ± 0.8	3.6 ± 1.0
145 – 135	257.403585	271	58	-2.89	–	blended	blended	blended	blended	blended	blended	blended
146 – 136	257.349180	350	116	-2.92	–	21.1 ± 1.2	38.9 ± 2.1	7.7 ± 1.0	5.1 ± 0.9	12.0 ± 1.3	12.7 ± 0.8	5.0 ± 0.6
147 – 137	257.284935	442	58	-2.96	–	9.6 ± 1.2	17.7 ± 2.0	–	blended	6.7 ± 0.6	4.6 ± 1.0	2.0 ± 0.6
148 – 138	257.210878	549	58	-3.00	–	7.3 ± 1.2	7.9 ± 2.6	–	3.5 ± 1.1	6.5 ± 1.2	–	3.4 ± 0.8
149 – 139	257.127036	670	116	-3.06	–	9.6 ± 0.8	21.0 ± 2.7	–	4.1 ± 1.1	10.0 ± 1.2	5.1 ± 0.9	4.6 ± 0.9
1410 – 1310	257.033444	806	58	-3.14	–	4.7 ± 1.1	–	–	–	–	–	–
1411 – 1311	256.930140	955	58	-3.25	–	1.6 ± 0.3	–	–	–	–	–	–

Notes. Three dots (...) indicate that a transition has not been observed, and a dash (–) indicates that a transition has not been detected.

Table B3. Spectroscopic parameters and integrated intensities for CH₃OH transitions used in the analysis.

Transition	Frequency (GHz)	E_{up} (K)	g_{up}	A_{ul} ($\log_{10}(\text{s}^{-1})$)	HBC494		HOPS-370		Per-emb-17		Per-emb-20		Ser-emb-8		Ser-emb-11W		Ser-emb-17	
6 ₋₂ - 7 ₋₁ , $v_t=0$; E	85.568131	75	52	-5.95	-	5.6 ± 1.1	-	-	-	0.9 ± 0.3	1.1 ± 0.3	-	-	-	-
7 ₋₂ - 6 ₋₃ , $v_t=0$; A	86.615574	103	60	-6.16	-	4.7 ± 1.0	-	-	-	-	1.7 ± 0.3	-	-	-	-
7 ₋₁ - 6 ₋₃ , $v_t=0$; A	86.902916	103	60	-6.16	-	5.0 ± 0.7	-	-	-	-	1.8 ± 0.3	-	-	-	-
15 ₃ ⁺ - 14 ₄ ⁺ , $v_t=0$; A	88.594787	328	124	-5.96	-	3.1 ± 1.0	-	-	-	-	1.8 ± 0.3	-	-	-	-
15 ₃ ⁻ - 14 ₄ ⁻ , $v_t=0$; A	88.939971	328	124	-5.95	-	6.1 ± 0.9	-	-	-	-	-	-	-	-	-
8 ₋₄ - 9 ₋₃ , $v_t=0$; E	89.505853	172	68	-6.12	-	5.6 ± 1.0	-	-	-	-	-	-	-	-	-
1 ₀ - 2 ₁ , $v_t=1$; E	93.196672	303	12	-5.38	-	-	-	-	-	-	2.0 ± 0.3	-	-	-	-
10 ₋₂ - 10 ₁ , $v_t=0$; E	102.122776	154	84	-6.76	-	-	-	-	-	-	1.3 ± 0.3	-	-	-	-
11 ₋₂ - 11 ₁ , $v_t=0$; E	102.658160	179	92	-6.58	-	-	-	-	-	0.8 ± 0.3	1.4 ± 0.3	-	-	-	-
12 ₋₂ - 12 ₁ , $v_t=0$; E	103.381258	207	100	-6.40	-	4.3 ± 0.9	-	-	-	-	1.8 ± 0.3	-	-	-	-
13 ₋₃ - 12 ₋₄ , $v_t=0$; E	104.060634	274	108	-5.80	-	6.6 ± 1.1	-	-	-	-	4.2 ± 0.3	-	-	-	-
11 ₋₁ - 10 ₋₂ , $v_t=0$; E	104.300337	159	92	-5.71	-	12.9 ± 1.0	-	-	-	-	5.0 ± 0.3	-	-	-	-
13 ₋₂ - 13 ₁ , $v_t=0$; E	104.336667	237	108	-6.23	-	7.3 ± 0.9	-	-	-	-	2.9 ± 0.3	-	-	-	-
10 ₄ ⁻ - 11 ₃ ⁻ , $v_t=0$; A	104.354831	208	84	-5.81	-	8.3 ± 0.9	-	-	-	-	2.3 ± 0.3	-	-	-	-
10 ₄ ⁺ - 11 ₃ ⁺ , $v_t=0$; A	104.410457	208	84	-5.80	-	8.7 ± 0.9	-	-	-	-	4.2 ± 0.3	-	-	-	-
13 ₁ ⁺ - 12 ₂ ⁺ , $v_t=0$; A	105.063816	224	108	-5.67	-	10.0 ± 1.0	-	-	-	2.1 ± 0.5	3.6 ± 0.3	-	-	-	-
14 ₋₂ - 14 ₁ , $v_t=0$; E	105.576396	270	116	-6.07	-	4.8 ± 1.0	-	-	-	-	2.0 ± 0.3	-	-	-	-
3 ₁ ⁺ - 4 ₀ ⁺ , $v_t=0$; A	107.013831	28	28	-5.21	-	20.3 ± 0.9	-	-	-	-	4.0 ± 0.3	-	-	-	3.9 ± 0.9
15 ₋₂ - 15 ₁ , $v_t=0$; E	107.159906	305	124	-5.92	-	5.6 ± 1.0	-	-	-	-	2.0 ± 0.3	-	-	-	-
1 ₁ ⁺ - 2 ₀ ⁺ , $v_t=0$; A	205.791270	17	12	-4.47	-	13.7 ± 0.4	22.9 ± 1.3	-	-	-	-	-	-	-	-	3.6 ± 0.9
12 ₅ - 13 ₄ , $v_t=0$; E	206.001302	317	100	-4.98	-	8.4 ± 1.1	13.7 ± 1.5	-	-	-	-	3.6 ± 0.7	-	-	-	-
19 ₁ - 19 ₀ , $v_t=0$; E	209.518804	462	156	-4.50	-	13.1 ± 0.9	16.3 ± 1.4	-	-	-	-	5.3 ± 0.8	-	-	-	-
4 ₂ - 3 ₁ , $v_t=0$; E	218.440063	46	36	-4.33	-	12.8 ± 0.6	47.4 ± 1.4	-	-	3.5 ± 1.2	-	5.0 ± 0.7	-	-	-	blended
8 ₀ - 7 ₁ , $v_t=0$; E	220.078561	97	68	-4.60	-	16.0 ± 0.6	39.5 ± 1.6	-	-	3.7 ± 1.0	-	4.0 ± 0.8	-	-	-	3.0 ± 0.8
16 ₂ ⁺ - 15 ₁ ⁺ , $v_t=1$; A	222.722856	613	132	-4.44	-	4.4 ± 0.6	6.6 ± 1.6	-	-	-	-	2.7 ± 0.8	-	-	-	-
20 ₋₂ - 19 ₋₃ , $v_t=0$; E	224.699408	514	164	-4.70	-	8.5 ± 0.5	12.3 ± 1.3	-	-	-	-	4.2 ± 0.9	-	-	-	-
5 ₃ ⁻ - 4 ₃ ⁻ , $v_t=2$; A	240.916172	693	44	-4.41	-	2.9 ± 0.2 *	2.9 ± 0.4 *	-	-	-	3.4 ± 0.3 *	3.8 ± 0.4 *	-	-	-	2.8 ± 0.5 *
5 ₃ ⁺ - 4 ₃ ⁺ , $v_t=2$; A	240.916173	693	44	-4.41	-	2.9 ± 0.2 *	2.9 ± 0.4 *	-	-	-	3.4 ± 0.3 *	3.8 ± 0.4 *	-	-	-	2.8 ± 0.5 *
5 ₀ ⁺ - 4 ₋₁ , $v_t=1$; E	241.238144	448	44	-4.24	-	11.5 ± 0.7	17.2 ± 1.6	-	-	4.4 ± 0.8	-	9.7 ± 1.0	-	-	-	-
5 ₀ ⁺ - 4 ₀ ⁺ , $v_t=1$; A	241.267862	458	44	-4.22	-	10.8 ± 0.6	15.0 ± 1.5	-	-	-	6.1 ± 1.2	10.3 ± 0.9	-	-	-	6.8 ± 1.1
5 ₁ ⁻ - 4 ₁ ⁻ , $v_t=2$; A	241.364143	718	44	-4.24	-	blended	-	-	-	-	-	6.7 ± 0.9	-	-	-	-
5 ₁ ⁻ - 4 ₁ ⁻ , $v_t=1$; A	241.441270	360	44	-4.24	-	13.5 ± 0.6	26.6 ± 1.4	-	-	3.8 ± 0.8	11.7 ± 1.2	14.0 ± 0.9	-	-	-	-
25 ₃ ⁻ - 25 ₂ ⁻ , $v_t=0$; A	241.588758	804	204	-4.09	-	7.4 ± 0.6	11.6 ± 1.9	-	-	-	5.3 ± 1.2	10.2 ± 0.9	-	-	-	-
5 ₀ - 4 ₀ , $v_t=0$; E	241.700159	48	44	-4.22	-	4.4 ± 0.8	blended	blended	blended	blended	29.1 ± 1.8	blended	blended	blended	blended	blended
5 ₋₁ - 4 ₋₁ , $v_t=0$; E	241.767234	40	44	-4.24	-	5.7 ± 1.0	blended	blended	blended	blended	43.5 ± 4.9	blended	blended	blended	blended	blended
5 ₀ ⁺ - 4 ₀ ⁺ , $v_t=0$; A	241.791352	35	44	-4.22	-	4.9 ± 1.0	115.8 ± 1.3	16.4 ± 1.1	10.7 ± 1.0	16.4 ± 1.1	43.8 ± 5.0	19.7 ± 1.0	-	-	-	9.0 ± 1.6
5 ₄ ⁻ - 4 ₄ ⁻ , $v_t=0$; A	241.806524	115	44	-4.66	-	blended	blended	blended	blended	blended	2.5 ± 0.5 *	blended	blended	blended	blended	blended

Table B3 *continued*

Table B3 (continued)

Transition	Frequency (GHz)	E_{up} (K)	g_{up}	A_{ul} ($\log_{10}(\text{s}^{-1})$)	HBC494	HOPS-370	Per-emb-17	W (K km s $^{-1}$)			Ser-emb-17
								Per-emb-20	Ser-emb-1	Ser-emb-8	
$5_1^+ - 4_1^+$, $v_t=0$; A	241.806525	115	44	-4.66	—	blended	blended	blended	2.5 ± 0.5 *	blended	blended
$5_{-4} - 4_{-4}$, $v_t=0$; E	241.813255	123	44	-4.66	—	blended	blended	blended	4.3 ± 1.0	blended	blended
$5_1 - 4_1$, $v_t=0$; E	241.879025	56	44	-4.22	—	blended	blended	blended	8.0 ± 0.9	blended	blended
$5_2^+ - 4_2^+$, $v_t=0$; A	241.887674	72	44	-4.29	3.7 ± 0.5	blended	blended	blended	7.0 ± 0.9	blended	blended
$14_{-1} - 13_{-2}$, $v_t=0$; E	242.446084	249	116	-4.64	—	21.3 ± 1.3	51.0 ± 2.6	blended	2.8 ± 0.9	blended	15.6 ± 1.3
$24_5^- - 24_5^+$, $v_t=0$; A	242.490245	746	196	-4.09	—	9.3 ± 1.3	13.9 ± 2.6	—	—	—	10.3 ± 1.2
$18_6^- - 19_5^+$, $v_t=0$; A	243.397393	590	148	-4.70	—	4.2 ± 0.1 *	7.2 ± 1.1 *	—	—	3.7 ± 0.6 *	5.2 ± 0.5 *
$18_6^+ - 19_5^+$, $v_t=0$; A	243.397654	590	148	-4.70	—	4.2 ± 0.1 *	7.2 ± 1.1 *	—	—	3.7 ± 0.6 *	5.2 ± 0.5 *
$23_3^- - 23_2^+$, $v_t=0$; A	243.412610	690	188	-4.09	—	9.5 ± 0.2	16.3 ± 2.2	—	—	—	10.6 ± 1.1
$5_1^- - 4_1^-$, $v_t=0$; A	243.915788	50	44	-4.22	—	26.8 ± 0.7	101.0 ± 1.7	blended	13.9 ± 1.1	20.9 ± 1.1	11.9 ± 0.8
$18_{-6} - 17_{-7}$, $v_t=1$; E	245.094503	889	148	-4.68	—	blended	—	—	—	3.6 ± 0.7	—
$21_3^- - 21_2^+$, $v_t=0$; A	245.223019	586	172	-4.08	—	13.8 ± 1.0	28.9 ± 1.5	blended	4.6 ± 0.9	10.5 ± 0.9	15.3 ± 0.9
$20_3^- - 20_2^+$, $v_t=0$; A	246.074605	537	164	-4.08	—	17.7 ± 1.0	36.1 ± 1.3	blended	6.0 ± 0.9	13.4 ± 0.8	18.2 ± 0.8
$19_3^- - 19_2^+$, $v_t=0$; A	246.873301	491	156	-4.08	—	17.7 ± 1.0	41.0 ± 1.9	blended	8.9 ± 0.9	9.8 ± 0.8	14.0 ± 0.8
$16_2^- - 15_3^+$, $v_t=0$; E	247.161950	338	132	-4.59	—	19.2 ± 1.4	42.7 ± 1.4	blended	5.1 ± 0.8	blended	14.2 ± 0.8
$4_2^+ - 5_1^+$, $v_t=0$; A	247.228587	61	36	-4.67	—	21.9 ± 1.4	64.8 ± 1.4	blended	5.5 ± 0.8	15.5 ± 0.9	14.0 ± 0.8
$18_3^- - 18_2^+$, $v_t=0$; A	247.610918	447	148	-4.08	—	19.6 ± 1.4	49.0 ± 2.2	blended	7.2 ± 0.6	11.3 ± 0.9	13.4 ± 0.7
$12_{-2} - 13_{-3}$, $v_t=1$; E	247.840050	545	100	-4.20	—	12.7 ± 0.7	27.1 ± 1.7	blended	—	blended	12.2 ± 0.9
$23_1 - 23_0$, $v_t=0$; E	247.968119	661	188	-4.35	—	8.6 ± 0.9	13.8 ± 1.7	blended	—	5.6 ± 0.7	8.7 ± 0.9
$17_3^- - 17_2^+$, $v_t=0$; A	248.282424	405	140	-4.08	—	20.3 ± 0.3	59.2 ± 1.9	blended	8.3 ± 0.8	12.6 ± 1.1	13.6 ± 1.0
$19_3^+ - 19_2^-$, $v_t=0$; A	258.780248	491	156	-4.05	—	13.3 ± 0.5	50.4 ± 1.9	blended	8.1 ± 1.0	blended	14.3 ± 1.0
$17_2^- - 16_1^-$, $v_t=1$; A	259.273686	653	140	-4.25	—	8.3 ± 0.7	18.4 ± 2.0	blended	—	7.5 ± 1.0	9.0 ± 0.9
$24_1 - 24_0$, $v_t=0$; E	259.581398	717	196	-4.31	—	6.8 ± 1.4	14.6 ± 1.6	blended	—	blended	blended
$20_{-8} - 21_{-7}$, $v_t=0$; E	260.064318	808	164	-4.67	—	—	—	blended	—	7.2 ± 1.1	—
$20_3^+ - 20_2^-$, $v_t=0$; A	260.381463	537	164	-4.04	—	15.4 ± 1.2	52.7 ± 2.3	blended	7.7 ± 1.0	18.2 ± 1.4	15.6 ± 1.2
$21_{-4} - 20_{-5}$, $v_t=0$; E	261.061320	624	172	-4.52	—	7.4 ± 1.1	12.5 ± 2.0	blended	—	4.2 ± 0.8	5.7 ± 0.8
$12_6 - 13_5$, $v_t=0$; E	261.704409	360	100	-4.75	—	blended	blended	blended	—	8.2 ± 1.1	9.6 ± 1.0
$2_1 - 1_0$, $v_t=0$; E	261.805675	28	20	-4.25	—	19.0 ± 0.3	99.6 ± 2.2	blended	12.1 ± 1.0	17.7 ± 0.9	14.8 ± 1.2
$21_3^+ - 21_2^-$, $v_t=0$; A	262.223872	586	172	-4.03	—	11.8 ± 0.9	40.0 ± 1.9	blended	5.1 ± 0.7	12.4 ± 1.0	8.6 ± 0.9

Notes. Only transitions that are detected and not blended toward at least one source in the sample are listed. Three dots (. . .) indicate that a transition has not been observed, and a dash (-) indicates that a transition has not been detected. Integrated intensities marked with an asterisk (*) are obtained by dividing the integrated intensity for two blended transitions with equal spectroscopic parameters by two.

C. ROTATION AND POPULATION DIAGRAMS

Rotation diagrams for CH_3CN are shown in Fig. C1, and population diagrams for the $14_K - 13_K$, $14_K - 13_K$ and $14_K - 13_K$ transitions are presented in Fig. C2, Fig. C3 and Fig. C4, respectively. Rotation diagrams for CH_3OH are shown in Fig. C5, and population diagrams for the emission at 1 mm, 2 mm and 3 mm are displayed in Fig. C6, Fig. C7 and Fig. C8, respectively.

D. ADDITIONAL FIGURES

Figure D1 presents the $\tau = 1$ contours for the $J_K = 5_K - 4_K$ transitions as well as the $5_2 - 4_2 / 5_4 - 4_4$ line ratio as function of column density and excitation temperature for emission in LTE. In addition, Fig. D2 presents NOEMA spectra for the HC^{15}N $J = 3 - 2$ transition toward the sources in our sample as obtained in the 1 mm observations.

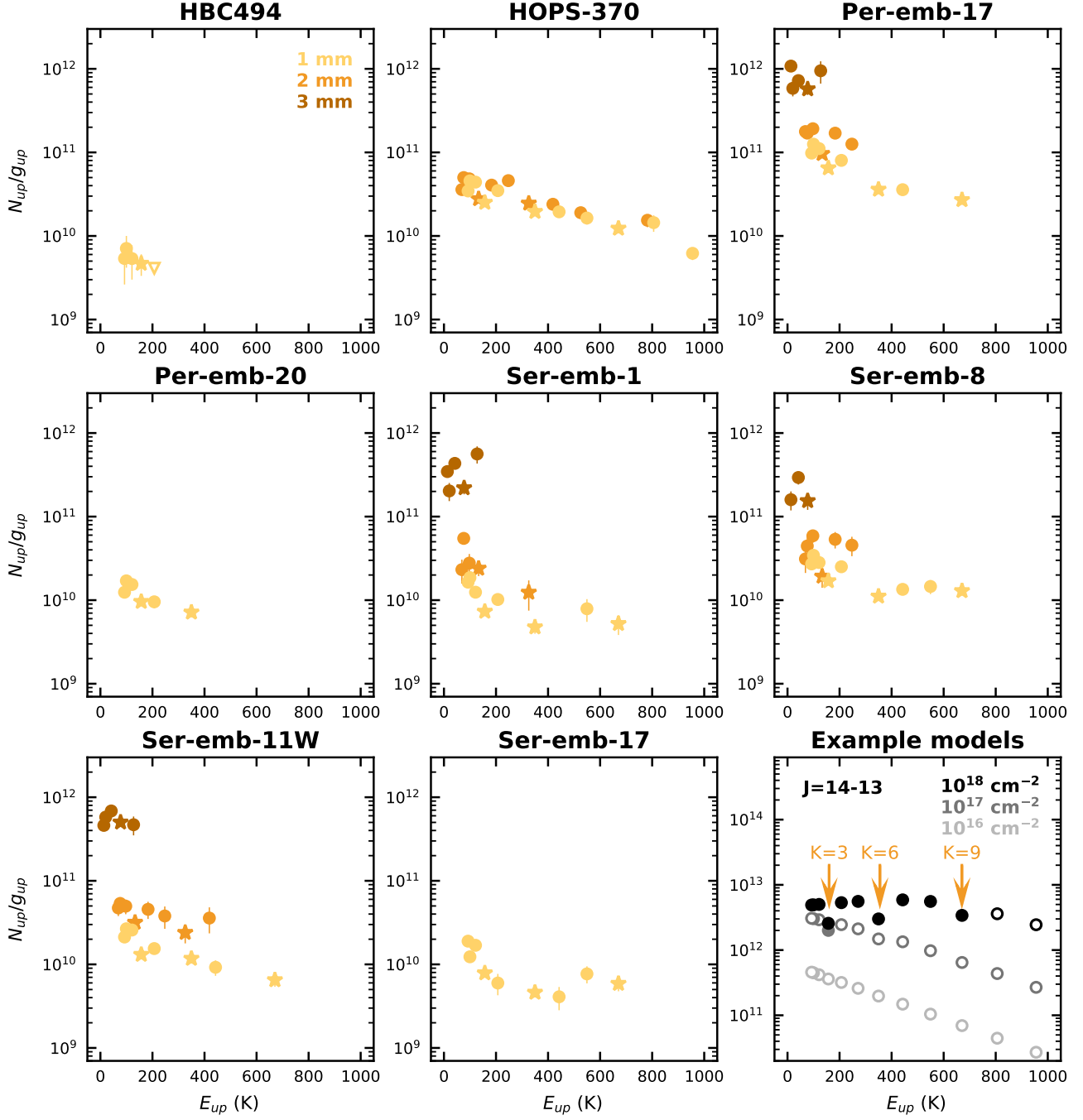


Figure C1. Rotation diagrams for the CH_3CN $J = 5 - 4$ (dark orange), $J = 12 - 11$ (orange), and $J = 14 - 13$ (yellow) ladders toward the sources in our sample as indicated above each panel. The $K = 3$, $K = 6$ and $K = 9$ transitions are shown as star symbols, the other transitions are shown as circles. The unresolved $12_K - 11_K$ and $5_K - 4_K$ fluxes have been scaled to the smaller beam size of the unresolved $14_K - 13_K$ observations. The vertical scale is the same for all panels, but the beam size differs per source (see Table 2). The error bars correspond to 1σ , and are typically smaller than the symbols. The bottom right panel displays three LTE models for the $J = 14 - 13$ ladder at 300 K with varying column densities (different shades of gray), highlighting the behavior of the $K = 3$, $K = 6$ and $K = 9$ transitions when the emission becomes optically thick. Optically thin transitions in this panel are shown as open symbols, and optically thick transitions as filled symbols.

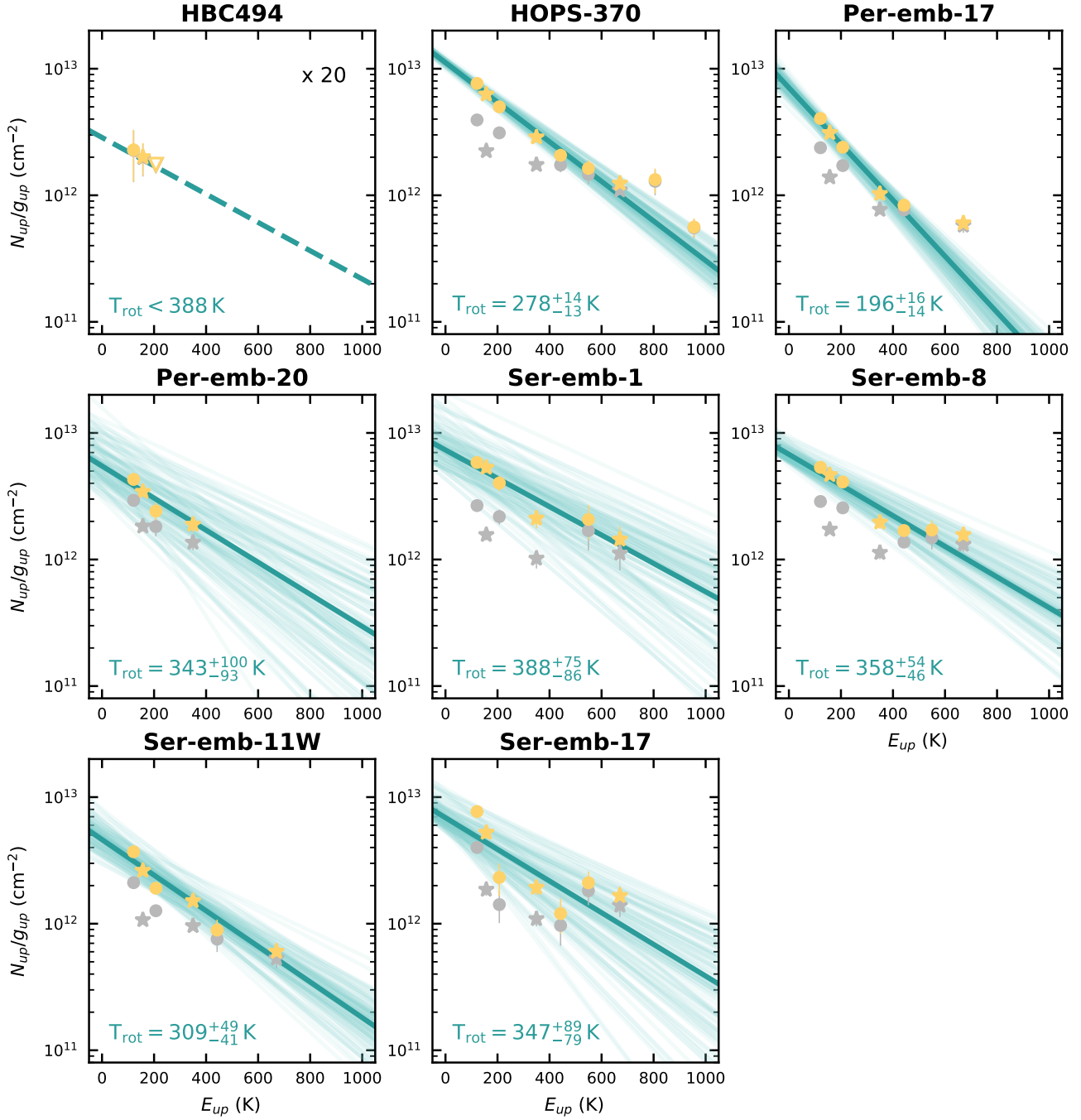


Figure C2. Population diagram analysis for $\text{CH}_3\text{CN } J = 14 - 13$. Data points corrected for source size are shown in grey, data points corrected for source size and optical depth are shown in yellow. The blended $K = 0$ and $K = 1$ transitions are excluded in the modeling and not depicted here. $K = 3$, $K = 6$ and $K = 9$ transitions are shown as star symbols, the other transitions are shown as circles. For HBC494, the values are multiplied by a factor 20 to allow the same vertical scale for all panels, and the triangle denotes the marginal detection of the $K = 4$ transition. The error bars correspond to 1σ , and are typically smaller than the symbols. The rotational temperature, column density and source size were fitted, except for HBC494 where the source size was fixed. Draws from the fit posteriors are shown with light teal lines, with the 50th percentiles shown as thick teal lines. The corresponding rotational temperature is listed in the bottom left corner. All fit results are presented in Table 3.

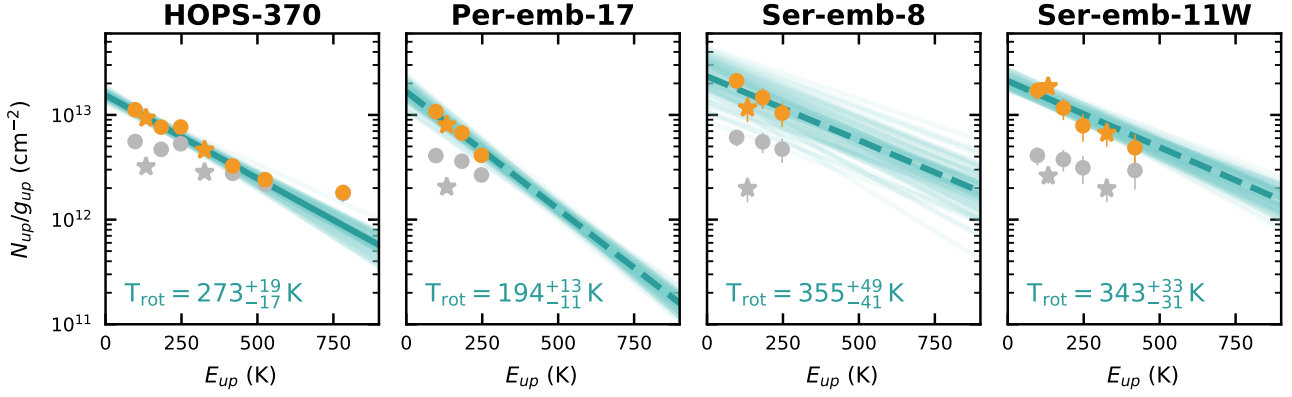


Figure C3. As Fig. C2 but for $\text{CH}_3\text{CN } J = 12 - 11$. Solid thick teal lines indicate that the rotational temperature, column density and source size were included in the fit, while a dashed line indicates that the source size was fixed. More details and all fit results are presented in Table 3.

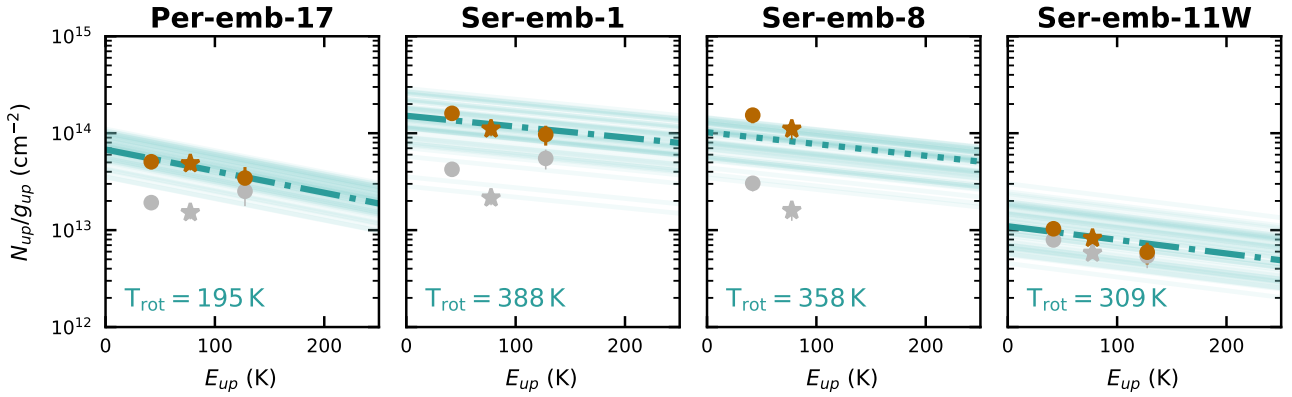


Figure C4. As Fig. C2 but for $\text{CH}_3\text{CN } J = 5 - 4$. Dash-dotted lines indicate that the column density and source size were included in the fit while the rotational temperature was fixed, while dotted lines indicate that both the rotational temperature and source size were fixed. More details and all fit results are presented in Table 3.

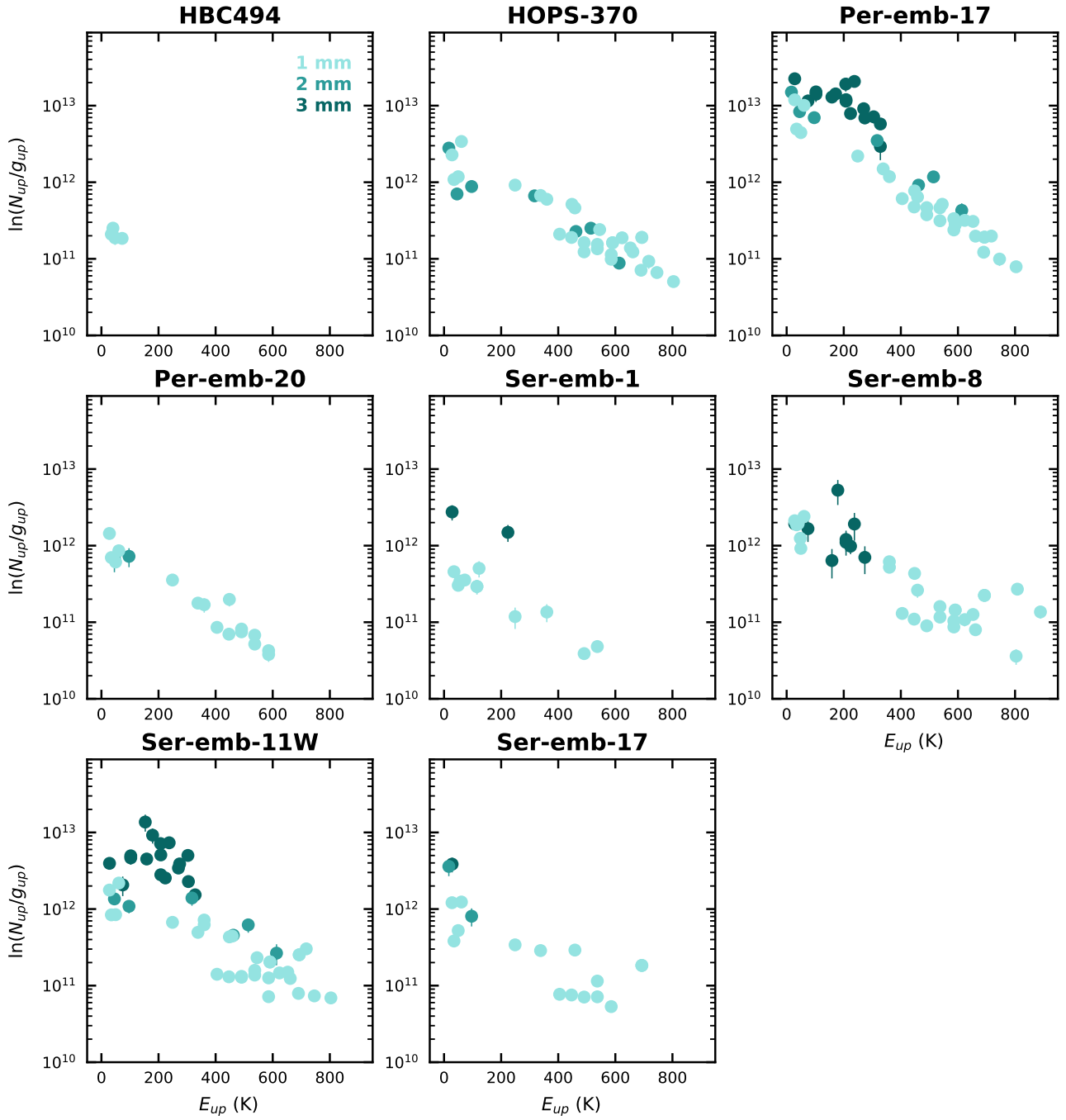


Figure C5. Rotation diagrams for CH_3OH at 1 mm (light teal), 2 mm (teal) and 3 mm (dark teal) toward the sources in our sample as indicated above each panel. The unresolved fluxes at 2 and 3 mm have been scaled to the smaller beam size of the 1 mm observations. The vertical scale is the same for all panels, but the beam size differs per source (see Table 2). The error bars correspond to 1σ , and are typically smaller than the symbols.

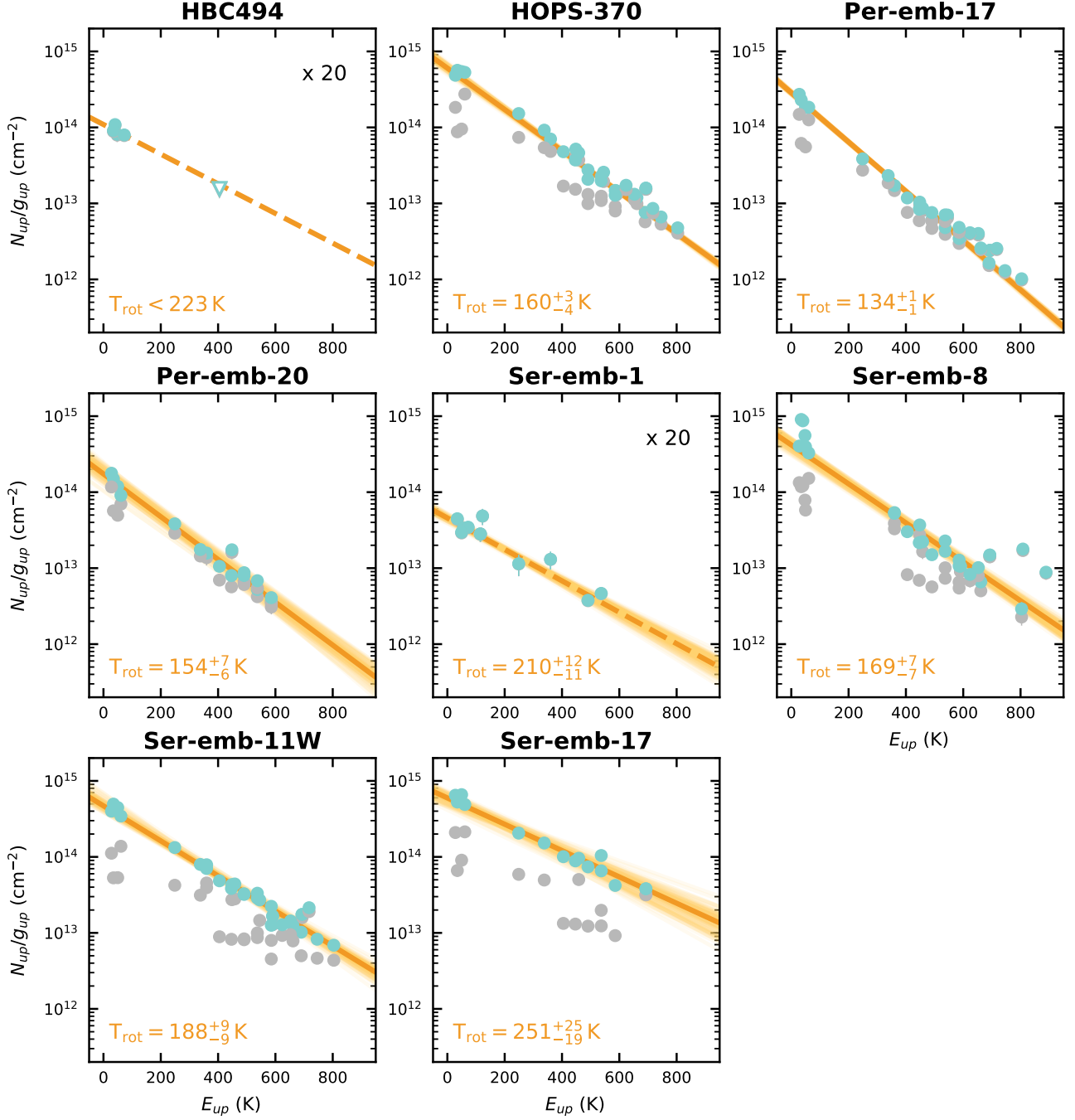


Figure C6. As Fig. C2 but for the 1 mm CH_3OH transitions. Values for HBC494 and Ser-emb-1 have been multiplied by 20 to allow the same vertical scale for all panels. For HBC494, the triangle denotes the most constraining upper limit of all covered transitions. Solid thick orange lines indicate that the rotational temperature, column density and source size were included in the fit, while a dashed line indicates that the source size was fixed. More details and all fit results are presented in Table 4.

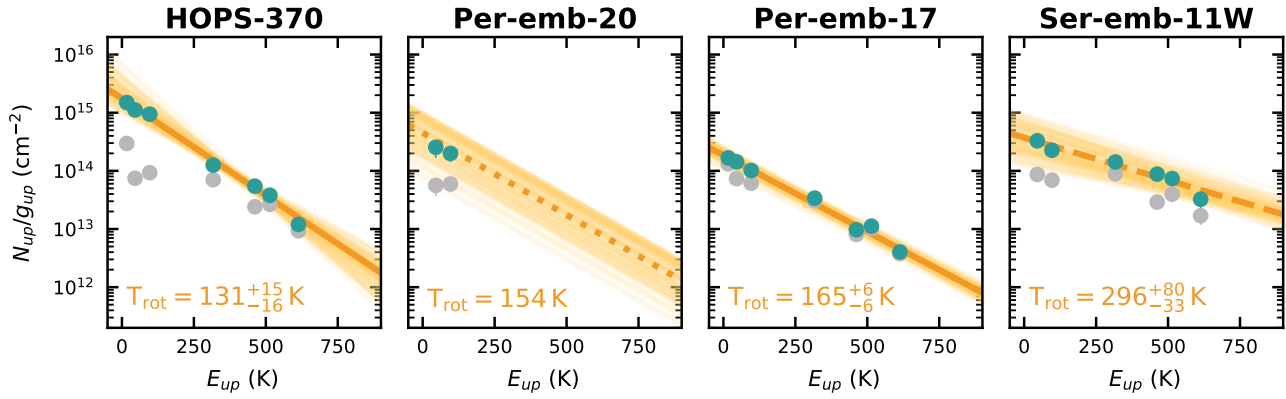


Figure C7. As Fig. C2 but for the 2 mm CH₃OH transitions. Solid thick orange lines indicate that the rotational temperature, column density and source size were included in the fit, while a dashed line indicates that the source size was fixed and a dotted line means that both the source size and rotational temperature were fixed. More details and all fit results are presented in Table 4.

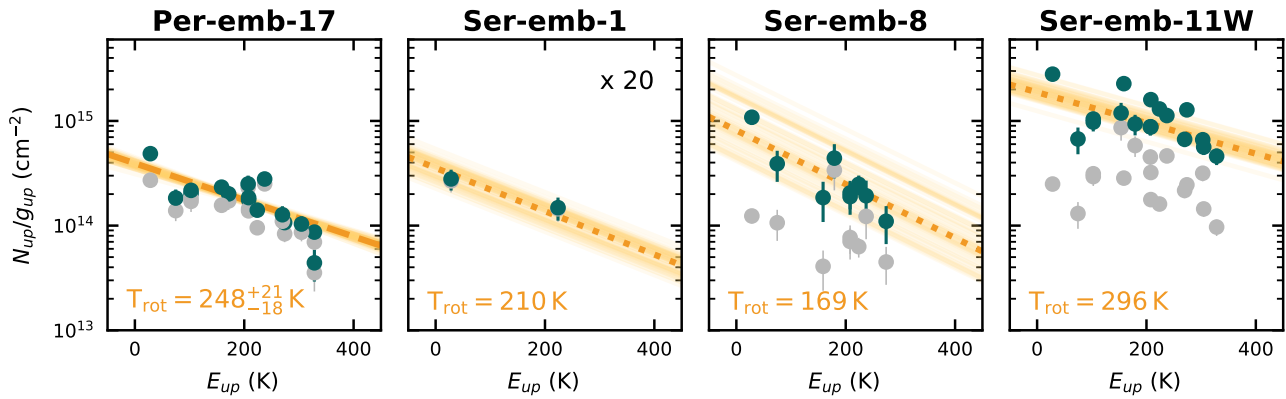


Figure C8. As Fig. C2 but for the 3 mm CH₃OH transitions. Values for Ser-emb-1 have been multiplied by 20 to allow the same vertical scale for all panels. Dashed lines indicate that the rotational temperature and column density were included in the fit while the source size was fixed. Dotted lines indicate that both the rotational temperature and source size were fixed. More details and all fit results are presented in Table 4.

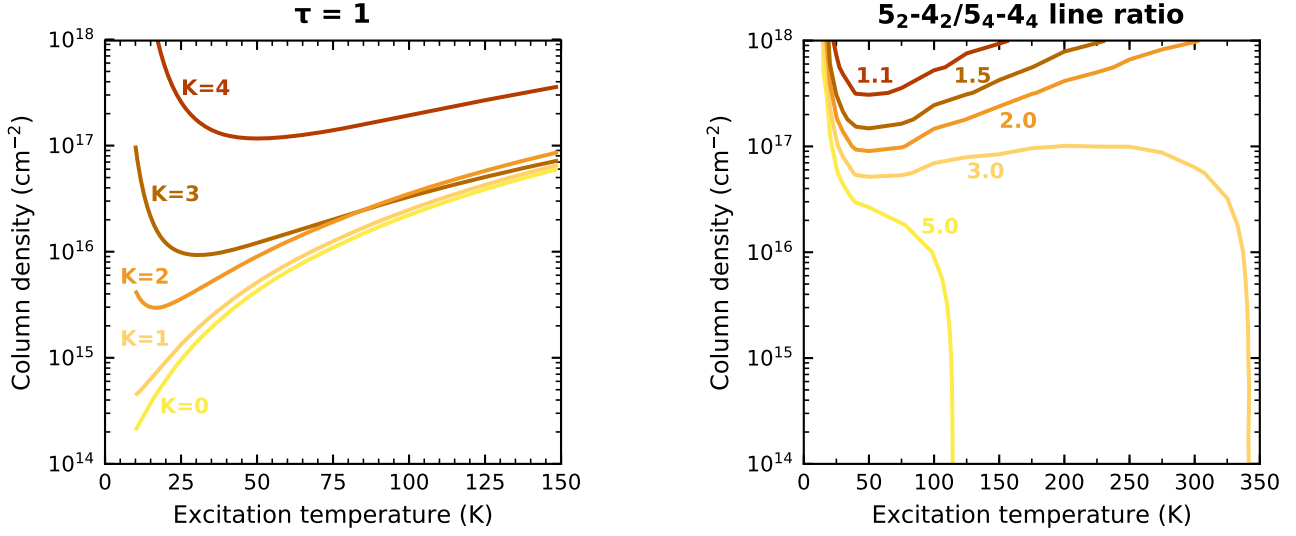


Figure D1. $\tau=1$ contours for the different K -components of the $\text{CH}_3\text{CN } J = 5 - 4$ ladder (left panel) and the $\text{CH}_3\text{CN } 5_2 - 4_2/5_4 - 4_4$ line ratio (right panel) for emission in LTE as function of column density and excitation temperature. A line width of 8.4 km s^{-1} has been adopted (as observed toward Per-emb-17). Observed $5_2 - 4_2/5_4 - 4_4$ line ratios range between ~ 1.5 – 3.0 for the sources in our sample.

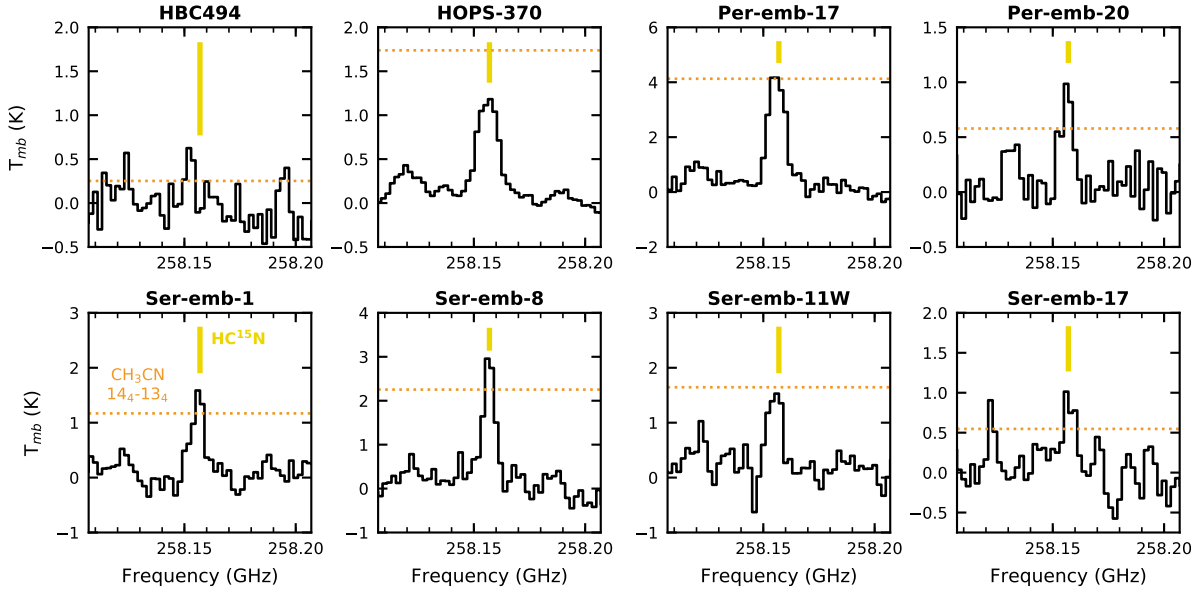


Figure D2. Spectra of the $\text{HC}^{15}\text{N } J = 3 - 2$ transition toward the sources in our sample. The line frequency is marked with a yellow vertical line, and the horizontal dotted orange line marks the peak brightness temperature of the $\text{CH}_3\text{CN } 14_4 - 13_4$ transition in that source.